Uranium (VI) Adsorbate Structures on Portlandite [Ca(OH)2] Type Surfaces Determined by Computational Modelling and X-ray Absorption Spectroscopy

Document Version
Final published version

[Link to publication record in Manchester Research Explorer](#)

OPEN ACCESS

Article

Uranium (VI) Adsorbate Structures on Portlandite [Ca(OH)$_2$] Type Surfaces Determined by Computational Modelling and X-ray Absorption Spectroscopy

Christopher A. Lee [1], Arjen van Veelen [2], Katherine Morris [3], J. Fred W. Mosselmans [4], Roy A. Wogelius [3,*] and Neil A. Burton [5,*]

[1] National Nuclear Laboratory Limited, NNL, Abingdon, Oxfordshire OX14 3DB, UK; christopher.lee@uknnl.com
[2] Material Science and Technology Division, Los Alamos National Laboratory, Los Alamos, NM 87545, USA; arjen.vanveelen@lanl.gov
[3] Department of Earth and Environmental Sciences, University of Manchester, Manchester M13 9PL, UK; katherine.morris@manchester.ac.uk
[4] Diamond Light Source, Didcot OX11 0DE, UK; fred.mosselmans@diamond.ac.uk
[5] Department of Chemistry, University of Manchester, Manchester M13 9PL, UK
* Correspondence: roy.wogelius@manchester.ac.uk (R.A.W.); neil.burton@manchester.ac.uk (N.A.B.)

Abstract: Portlandite [Ca(OH)$_2$] is a potentially dominant solid phase in the high pH fluids expected within the cementitious engineered barriers of Geological Disposal Facilities (GDF). This study combined X-ray Absorption Spectroscopy with computational modelling in order to provide atomic-scale data which improves our understanding of how a critically important radionuclide (U) will be adsorbed onto this phase under conditions relevant to a GDF environment. Such data are fundamental for predicting radionuclide mass transfer. Surface coordination chemistry and speciation of uranium with portlandite [Ca(OH)$_2$] under alkaline groundwater conditions (ca. pH 12) were determined by both in situ and ex situ grazing incidence extended X-ray absorption fine structure analysis (EXAFS) and by computational modelling at the atomic level. Free energies of sorption of aqueous uranyl hydroxides, [UO$_2$(OH)$_n$]$^{2-n}$ (n = 0–5) with the (001), (100) and (203) or (101) surfaces of portlandite are predicted from the potential of mean force using classical molecular umbrella sampling simulation methods and the structural interactions are further explored using fully periodic density functional theory computations. Although uranyl is predicted to only weakly adsorb to the (001) and (100) clean surfaces, there should be significantly stronger interactions with the (203/101) surface or at hydroxyl vacancies, both prevalent under groundwater conditions. The uranyl surface complex is typically found to include four equatorially coordinated hydroxyl ligands, forming an inner-sphere sorbate by direct interaction of a uranyl oxygen with surface calcium ions in both the (001) and (203/101) cases. In contrast, on the (100) surface, uranyl is sorbed with its axis more parallel to the surface plane. The EXAFS data are largely consistent with a surface structural layer or film similar to calcium uranate, but also show distinct uranyl characteristics, with the uranyl ion exhibiting the classic dioxygenyl oxygens at 1.8 Å and between four and five equatorial oxygen atoms at distances between 2.28 and 2.35 Å from the central U absorber. These experimental data are wholly consistent with the adsorbate configuration predicted by the computational models. These findings suggest that, under the strongly alkaline conditions of a cementitious backfill engineered barrier, there would be significant uptake of uranyl by portlandite to inhibit the mobility of U(VI) from the near field of a geological disposal facility.

Keywords: portlandite; uranyl; adsorption; hyperalkaline; extended X-ray absorption fine structure (EXAFS); potential of mean force (PMF); molecular dynamics (MD); density functional theory (DFT)

1. Introduction

The interaction of radionuclides with cementitious engineered barrier systems and the surrounding mineral environment is of fundamental importance for the safe disposal of intermediate-level radioactive wastes [1]. Typically, the most ubiquitous radionuclide by mass in intermediate-level wasteforms to be disposed of will be uranium. In its higher oxidation state, U(VI) can be readily solubilised in aqueous conditions and complexes of uranyl ions (UO_2^{2+}) have the potential to be highly mobile [2]. Additionally, under the high pH and mildly reduced conditions associated with cementitious geological disposal, U(VI) is reportedly stabilised [3].

This study will focus on the higher pH environments anticipated over the longer term in intermediate-level waste geological disposal facilities (GDF) which, in many cases, will rely upon cement-based backfills and wasteforms to prevent or limit the migration of the radionuclides to the wider environment. Typical cement degradation conditions are highly alkaline, ranging from pH > 10 in CSH gels through to pH 13 when KOH/NaOH dominate dissolution. Portlandite [$Ca(OH)_2$] is a potentially significant mineral surface in these materials during the period that intermediate-level wasteforms (ILW) will be emplaced, and there is a paucity of quantitative understanding of how the waste species will interact or be retarded by this mineral phase. The extreme pH conditions expected in the most proximate conditions in a GDF are the most difficult to model or access experimentally, so these conditions are the focus of this study. Thus, a detailed and critical understanding of the uptake of uranyl (VI) ions by portlandite is important in any safety case for a cementitious GDF. The objective of this study is to determine adsorbate structures under extremely high pH conditions for uranium on reactive hydroxylated portlandite-type surfaces.

In order to better understand the nature of the interactions of uranium with portlandite, we have employed both experimental grazing incidence X-ray absorption spectroscopy and computational modelling at the atomic level. Our computational models have been constructed to assess the interactions that might be expected under aqueous conditions with pH circa 12 (the point of zero charge pH ~12.7 of portlandite [4]) and where, in the absence of high concentrations of carbonate, the uranyl hydroxides [$UO_2(OH)_n$]$^{2-n}$ (*n* = 0–5) will be the dominant species.

We shall show that, although we might expect the kinetics and surface chemistry of portlandite to be relatively simple, there are a wide range of specific U(VI) interactions to consider. Specifically, precipitation, recrystallization or incorporation of U(VI) near the surface are likely since sorption of uranyl ions is particularly favourable on roughened surfaces exposed to an aqueous environment.

Galmarini et al. [5] have shown that whilst the (001) surface of portlandite is the most stable in the gas phase, the (101) surface [6] (originally identified as the similar (203) surface), is the most stable in aqueous solutions. This latter surface is of particular interest here, as it implies that surface calcium ions are exposed to solvent, rather than a dense hydroxyl layer, and these may act as possible enhanced binding sites for uranyl hydroxide anionic species.

Potentials of mean force, which allow us to determine the free energy of adsorption of the uranyl species under aqueous conditions, have been computed for the three main surfaces of portlandite: (001), (100) and (101). In addition, adsorption will be considered in the region of hydroxyl vacancy defects of these solvated surfaces, including a step on the (101) surface (i.e., 203 plane), to better understand potentially less ideal conditions. Density functional theory is then applied to some configurations for a more accurate assessment of the inner-sphere interactions of uranyl with the surface—in particular, whether uranyl has a tendency to be retained perpendicular to the surface (interacting via the axial oxygen) or in a more parallel fashion (with the surface substituting for equatorial ligands).

Interactions of uranyl complexes with mineral surfaces: Uranyl has a propensity for uptake to a variety of common mineral surfaces, such as the carbonates including calcite or aragonite [7,8], silicates [9–11] and hydroxides such as brucite [12,13]. However, surprisingly, there has been relatively little research on the interactions of U(VI) with portlandite

[Ca(OH)$_2$], with previous studies focussing on modelling [14–17] or determining its structural properties [18–20] and crystal morphology [5,6]. This is in large part due to the experimental difficulties associated with the high solubility and rapid dissolution kinetics of both CaO and Ca(OH)$_2$. Despite these experimental challenges, information about surface-specific active sites is important in order to make predictions about how uranyl adsorbs and may be incorporated into the crystal structure. Previous experimental studies have examined the uptake of uranyl in batch experiments [21] and have also highlighted the relatively high uptake of U(VI) in degraded portlandite phases [22].

To that end, ex-situ and in-situ grazing incidence EXAFS (reflEXAFS) has been used in this study to constrain the adsorption of uranyl onto single crystal (hydroxylated) CaO(111), which, upon hydroxylation, will serve as a structural and chemical equivalent to the portlandite (001) surface. The advantage of this approach is that the data collected represents uranyl adsorption on one orientation so that the local coordination on a specific plane can be precisely constrained. Another advantage is that adsorption of U(VI) can be monitored in real time, which can give information about adsorption kinetics that otherwise would be lost in batch experiments.

Computational modelling can be a complementary aid to experimental approaches to model U(VI) uptake, and, in particular, atomistic molecular dynamics simulations and density functional theory quantum chemistry computations can provide direct atomic detail relating to the specific processes that take place. It is important to recognise that the properties of natural systems in equilibrium are those of thermodynamic ensembles, which are strongly dependent on a variety of possible atomic configurations over an extended timescale. Computationally, this will necessitate a range of computational models to be considered. The ligand exchange and sorption mechanisms are relatively rare events and are unlikely to occur within the pico- to nano-second timescales employed in molecular dynamics simulations [23]. The potential of mean force approach utilised in this study employs the constraint of a "reaction or collective coordinate" to mitigate some of these timescale limitations; however, although it does allow for some statistical sampling, we will only employ one reaction constraint in each simulation and a range of possible speciation models will need to be considered to describe the broader picture. We shall follow the general classical simulation approach utilised in previous sorption studies of uranyl on calcite [24,25], augmented by more accurate first-principles density functional theory calculations of a selection of inner-sphere complex models to probe potential surface-adsorbed states of uranyl. Essentially, the MD and PMF computations provide constraints on the free energy change associated with bringing the uranyl ion onto the mineral surface, with a range of values computed as a function of distance. This allows for a prediction of which surface statistically provides the lowest energy adsorbate layer. The DFT models then provide detailed information about the lowest energy chemical coordination structure for uranyl on each mineral surface of interest. Combining these two methods gives us complementary information about uranyl surface-attachment onto portlandite. Spectroscopic measurements then provide a test of the computational results and will allow us to confirm whether the computationally predicted configurations are discernible on real surfaces. Although the sorption of uranyl on portlandite has not been previously modelled, uranyl species have been shown to adsorb directly onto a range of related mineral surfaces, with a range of computational studies, including sorption of uranyl to calcite [24,26], montmorillonite [27], quartz [28], feldspar [29] and aluminosilicates [30]. These previous studies will be used to help constrain our experimental and computational observations.

2. Materials and Methods—Computational and Experimental Details

2.1. Atomistic Models

All computations are initially based upon the crystal structure of bulk portlandite determined by neutron diffraction [20], which has a rhombohedral structure with lattice parameters $a = b = 3.589$ Å, $c = 4.911$ Å, $\alpha = \beta = 90°$ and $\gamma = 120°$. In this work, classical simulations of the bulk structure or surfaces of portlandite used the force field of

Freeman et al. [31] and previously used by Galminari [5] to study its crystal morphology. Water was modelled using the four site TIP4P/2005 model [32] and uranyl was modelled using the parameters of Greathouse et al. [28], modified to include interactions with TIP4P/2005 water and portlandite. These force-field parameters are given in the supporting information.

The (001), (100) and (203) surfaces of portlandite were cleaved from the bulk unit cell using Accelrys Materials Studio [33] and a 50 Å vacuum gap was created above each surface to remove interactions between periodic images of the slab in the z-direction. A structure of 8×8 supercells of these surfaces was then generated, each eight $Ca(OH)_2$ layers thick (2560 atoms total), and the uranyl species $(UO_2(OH)_n^{2-n})$ $n = 0$–5 were placed into the vacuum gap. The cells were then solvated with TIP4P/2005 water and the whole system was equilibrated using classical molecular dynamics simulations at 298 K.

We note that the (203) surface in the simulation cell differs from a (101) surface by a single step; however, in all the non-defect surface computations, adsorption was not sampled in the vicinity of the step and all interactions were analogous to simulation on a pure (101) surface. Hence, we shall refer to computations involving this surface as (203/101) rather than (203). (See Figure S1 for a comparison of the (101) and (203) surfaces.)

Previous calcium oxide sorption experiments have shown that, particularly at high pH, the mineral surface will be rough and quite dynamic, with dissolution and re-crystallisation occurring at relatively short timescales [21]. In order to assess how uranyl sorption may be affected in this situation, a series of modified surfaces were modelled in which a point defect (vacancy) was created in each of the surfaces, (001) and (100), by removing a single hydroxide ion from the exposed face. In the case of the (203/101) surface, the vacancy was introduced into the step that occurs explicitly in the unit cell of the (203) surface and sorption was explicitly sampled around this site. We shall refer to the 3 defect surfaces as (001-OH), (100-OH) and (203-OH), respectively. Although we shall refer to the hydroxyl vacancies as defects, it should be borne in mind that the surfaces in our models are fully hydrated and any vacancy can be bound explicitly by water during equilibration, analogous to lower pH conditions where protonation of some of the hydroxyl surface is expected. Similarly, the (203/101) surfaces will be hydrated and water will solvate exposed calcium ions. Thus, an important differentiating feature of the (001), (100) and (203/101) model surfaces will be the density of hydroxyl groups: these are 0.0896 Å^{-2}, 0.0567 Å^{-2} and 0.1038 Å^{-2}, respectively.

2.2. Classical MD and PMF Simulations

Potential of mean force (PMF) calculations have been performed to predict the work (free energy) required to bring the 6 uranyl species, $[UO_2(OH)_n]^{2-n}$ ($n = 0$–5), from being fully solvated in solution towards and into contact with the three (001), (100) and (203/101) surfaces. For the defect surfaces, only the $UO_2(OH)_4^2$ complex was explicitly considered, although no specific restraints were included to maintain this coordination environment.

All classical molecular dynamics (MD) simulations were performed using DL_POLY Classic [34] with the PLUMED [35] plugin used to include the umbrella sampling potential. A timestep of 0.5 fs was used in all simulations. The simulations were all performed at a constant temperature of 298 K within the NVT ensemble using the Nose–Hoover [36] thermostat with a 0.1 ps relaxation time. Each simulation consisted of 100 ps for equilibration and 1 ns for production, during which statistics were collected.

A series of umbrella sampling molecular dynamics simulations were performed to compute a potential of mean force (PMF) to quantify the free energy of taking each uranyl complex from an aqueous solution to a surface. Our sampling protocols follow previous work using these techniques [24,37], where a harmonic potential of the form:

$$U = \frac{1}{2}k(\mathbf{r} - \mathbf{r}_0)^2 \tag{1}$$

was used to constrain the collective variable or reaction coordinate. For each PMF calculation, approximately 16 simulation windows were used, covering a coordinate that brings the uranyl complex from the solution to the surface of the slab, with additional windows added to improve the sampling in regions of high force. The coordinate was defined as the distance between the uranium atom and the centre of mass of the calcium atoms in the slab. The surface of the slab is defined as the z-coordinate of the hydrogen atoms at the exposed face of the slab in gas phase. The number of windows, the interval between each one and the value of the constraint parameter k varied such as to include a complete sampling of the reaction coordinate, with a value of k ranging from 0.5 to 3.0 eV. The weighted histogram analysis method [38,39] (WHAM) was used to combine and analyse the window distributions obtained from each simulation window and to calculate the free energy profile. Additional PMF simulations were performed to assess the hydroxyl–water ligand exchange energy (see Supplementary Materials for further details).

2.3. Density Functional Theory Calculations

Density Functional Theory calculations were mainly performed using CP2K (version 2.5.1) [40] with the PBE functional [41]. Core electrons were replaced by Goedecker–Teter–Hutter (GTH) pseudopotentials [42–44], while valence electrons were modelled using a mixed double-zeta Gaussian and plane wave basis [45]. Periodic boundary conditions were applied in all three dimensions.

Geometry optimisations were performed for models of the $UO_2(OH)_4^{2-}$ complex on clean (001, 100 and 203/101) and defect (001, 100 and 203) portlandite surfaces, with the uranyl axis either parallel or perpendicular to the surface (based on observed orientations from the classical trajectories). In each of these calculations, the surface slabs contained 8 $Ca(OH)_2$ layers that were analogous to the classical simulations, the absorbed complex was surrounded by thirty-eight explicit water molecules and periodic boundary conditions were applied.

In Table 1, we summarise a selection of gas-phase PBE functional structural optimisations with different functionals of $UO_2(OH)_4^{2-}$ in a typical conformation, very close in energy to the global minimum, observed in the simulations with 3 of the hydroxide H-atoms oriented in the same direction. EXAFS data from a previous study are included for comparison. These DFT calculations were performed using Gaussian 09 [46] with the pure PBE, hybrid PBE0, B3LYP and M06 functionals [47], a large-core SDD basis set and pseudopotential for uranium [48] and the 6-31G(d,p) basis set for oxygen, hydrogen and subsequently for Ca. We note, for later comparison to our EXAFS uranyl-portlandite distributions, that the PBE functional is likely to overestimate the U-O_{ax} bond lengths and U-O_{eq} bonds by around 0.03 and 0.02 Å, respectively, in agreement with previous work [49]. The r(U-O_{ax}) and r(U-O_{eq}) bond lengths of $UO_2(OH)_4^{2-}$ with PBE in the gas phase, or when water is implicitly included via the polarizable continuum model (PBE/PCM), are respectively 1.86 Å and 1.85 Å, or slightly longer than was observed experimentally in solution at 1.83 Å. We also note that hybrid functionals do result in shorter axial lengths and the equatorial bond lengths are slightly longer; unfortunately, the additional computational demands of these functionals precluded their use with the surface slab together with explicit water.

Two further gas-phase complexes were also considered (see Table 1) in order to give an estimate of the Ca-U and U-U interaction distances when Ca^{2+} directly interacts with $UO_2(OH)_4^{2-}$ or if $UO_2(OH)_4$ dimerises to $(UO_2)_2(OH)_6^{2-}$, in which there are 4 equatorial OH and 2 bridging OH groups. Dimerisation results in the U-O_{ax} and U-O_{eq} distances being shortened, with respect to the monomer, by 0.03 Å, and a U-U distance of 3.98 Å was predicted. The effect of the Ca^{2+} counter ion, binding with a Ca-U distance of 3.14 Å, is to lengthen the U-O_{ax} to which it directly interacts, and to shorten the other; the U-O_{eq} bonds to which the Ca^{2+} interacts are both considerably lengthened to about 2.50 Å and the remaining bonds slightly shortened.

Table 1. Optimised bond lengths (/Å) of $[UO_2(OH)_4]^{2-}$, $[(UO_2)_2(OH)_6]^{2-}$, $CaUO_2(OH)_4$ and U- or UO_2-incorporated portlandite structures using Density Functional Theory.

Model Structure	Functional	$R(U\text{-}O_{ax})$	$R(U\text{-}OH_{eq})$	$R(U\text{-}U)$	$R(Ca\text{-}U)$
$[UO_2(OH)_4]^{2-}$	PBE	1.861	2.298	-	-
	PBE0	1.810	2.286	-	-
	B3LYP	1.825	2.306	-	-
	M06	1.801	2.305	-	-
	PBE/PCM	1.853	2.277	-	-
	EXAFS [a]	1.83	2.26	-	-
$[(UO_2)_2(OH)_6]^{2-}$	PBE	1.825, 1.837	2.416–2.430 [b] 2.228–2.233	3.983	-
$CaUO_2(OH)_4$	PBE	1.805, 1.897	2.502, 2.506, 2.155, 2.158	-	3.141
U(VI)-substituted portlandite [c]	PBE	2.197	2.577	-	3.764
UO_2-substituted portlandite [d]	PBE	1.865, 1.867	2.259, 2.263, 2.261, 2.262	-	3.751, 3.755, 3.739, 3.749

[a] Experimental data from [50]. [b] For OH bridging the two uranyl groups. [c] U-portlandite is bulk portlandite with a Ca ion substituted with a U(VI) ion. O_{ax} are directly bonded to U, and O_{eq} bridge U-O-Ca. [d] $[UO_2(OH)_4]^{2-}$-portlandite is bulk portlandite with $Ca(OH)6$ substituted with $[UO_2(OH)_4]^{2-}$.

2.4. Experimental

Surface coordination chemistry and speciation of uranium were determined by both in-situ and ex-situ reflection geometry extended X-ray absorption fine structure analysis (reflEXAFS) on oriented hydroxylated single crystals of CaO (111), equivalent to the $Ca(OH)_2$ (001) surface. In order to obtain a surface similar to that of portlandite (001), commercially bought oriented single crystals of CaO (111) were used in this study and then hydroxylated. Oriented single crystals ($10 \times 10 \times 1$ mm) were produced, cut and polished by SurfaceNet GmbH Germany. The surface root mean square (RMS) starting roughness was between 20 and 30 Å.

2.4.1. Ex Situ Adsorption Experiments

A stock solution of 25,000 ppm natural UO_2Cl_2 was prepared. Two sets of experiments were completed (i) with 2 mM CO_3^{2-} and (ii) without CO_3^{2-}. In the first experiment, 1 mL (25 ppm) U(VI) of stock was spiked in a 2 mM K_2CO_3 solution. The pH was adjusted dropwise using HCl to pH 10.6 (± 0.1) to avoid the possible precipitation of compreignacite ($K_2(UO_2)_6O_4(OH)_6 \cdot 7H_2O$). The dominant uranium species in this solution would be $UO_2(CO_3)_3^{4-}$ (>99%, PHREEQC, SIT database [51]). The U(VI) solution was transferred into a centrifuge tube along with the crystal. The total contact time of the crystal solution was 48 h (± 2 h), after which the crystal was removed using Teflon-coated tweezers and wicked dry (without touching the crystal surface) to be transferred onto a domed sample holder suitable for reflEXAFS. The sample holder was then sealed using Kapton tape and bagged.

The second experiment involved spiking 0.4 mL (10 ppm) of U(VI) stock solution into a decarbonized pH 12 (0.01 M KOH) solution. Decarbonized water was obtained by boiling MilliQ water for one hour while purging it with N_2 gas. The dominant solute species were calculated to be ~51% $UO_2(OH)_3^-$ and ~49% $UO_2(OH)_4^{2-}$. During the reaction, the solution remained clear and no precipitate was formed. The total contact time of the crystal solution was 48 h (± 2 h), and it was then prepared as for experiment (i).

2.4.2. In Situ Adsorption Experiments

In line with the ex situ batch experiments, parallel solution chemistry was used here. In addition, an extra experiment with 10 ppm U(VI) at pH 12 in 0.01 M LiOH was used to further enhance the solubility of U(VI) at pH 12. These results were compared with the other experiments in order to account for any possible effects of compreignacite precipitation.

These experiments were performed at beam line I18 at Diamond Light Source Ltd., Didcot, UK. Real-time adsorption measurements were performed using a micro-fluid cell with a domed X-ray transparent window designed for actinide-bearing solutions. The sample cell was purged prior to reaction with N_2 gas. A syringe pump was connected to the cell using Teflon tubing and a reactant solution was input at a constant fluid flow rate of 1.5 mL/h for two hours. Uranium fluorescence-intensity data were collected during reaction in order to monitor surface uptake. After reaction, the surface was rinsed with 0.4 mL of CO_2 free MilliQ water at a flow rate of 1.5 mL/h and then purged with N_2 gas. This removed solute species of uranyl from the cell and left behind a thin film containing adsorbed uranyl.

2.4.3. reflEXAFS Measurements

Beam line I18 was configured to perform reflEXAFS. The beam line uses a Si (111) monochromator to select the energy of the beam, which was calibrated against the first derivative of yttrium (Y), defined at 17,038 eV. Fluorescence-yield data were collected using a four element Si drift Vortex detector, which was positioned vertically and directly above the crystal surface. Upstream vertical slits of 50 μm were used to define the incident beam.

Crystal alignment was achieved by first completing a rocking curve measurement so that the crystal surface was positioned flat and cutting half of the incident beam intensity. The angle of the crystal surface was then oriented to an incident angle of ~30 millidegrees, but in all cases kept below the critical angle of total external reflection so that the fluorescence signal remained optimized.

The EXAFS, $\chi(k)$, were refined from the raw data by standard procedures, including background subtraction, data normalization and fitting. Data analysis was performed using the software packages (d)Athena and (d)Artemis 0.9.18 [52].

3. Results

3.1. Bulk, Surface, and Uranium-Incorporated Portlandite

In order to assess the variance between the classical force-field and quantum DFT models, the bulk structure of portlandite was optimised using the PBE functional (Table S1). The force-field approach predicts lattice parameters of $a = b = 3.662$ Å and $c = 4.740$ Å, while DFT predicts $a = b = 3.644$ Å and $c = 4.993$ Å, both within a few percent of the literature values [19]. Surface energies of the (001), (100) and (203) surfaces (gas phase, i.e., with a vacuum gap) of portlandite were calculated using both the classical force-field and DFT (PBE) methods. The surface energy is calculated using

$$E_{surface} = \frac{E_{slab} - nE_{bulk}}{2S},\tag{2}$$

where E_{slab} is the energy of the slab, E_{bulk} is the energy of the bulk unit cell, n is the number of bulk units in the slab and S is the surface area of the slab defined as $AB \sin \gamma$, where A and B are the lengths of the A and B lattice vectors and γ is the angle between them. The surface energies (Tables S1–S3) for the two methods show the same trend with the (001) surface being the most stable in the gas phase and the classical values are in agreement with previous values [5].

An important consideration for the interaction of uranyl with portlandite is whether U(VI) can or will be incorporated within the bulk or surface layers of the mineral. Table 1 and Table S1 include the optimised results from the DFT (PBE) computations on two possible incorporated structures: (a) U-portlandite, where a single calcium(II) in a $5 \times 5 \times 5$ supercell of portlandite was substituted with a U(VI) ion and (b) $UO_2(OH)_4{}^{2-}$-portlandite, where a single $Ca(OH)_6$ unit was substituted by $UO_2(OH)_4{}^{2-}$. For the U(VI)-substituted portlandite model, the overall structure remains similar to pure portlandite with supercell lattice parameters $a = b = 17.945$ and $c = 24.555$ (Table S1) and U-O distances of 2.197 Å and 2.577 Å (Table 1), compared to the corresponding Ca-O distance of 2.363 Å in bulk portlandite [17]. For the UO_2 substituted-portlandite system, the optimized supercell lattice parameters are

a = 18.189 Å and *c* = 24.700 Å (Table S1), again almost identical to those predicted for bulk portlandite. However, importantly in this case, without the two protons to form hydroxyl, the complex retains its uranyl character but is distorted with U-O$_{ax}$ and U-OH distances of 1.87 Å and 2.26 Å, respectively, while the U-Ca distances are 3.751 Å, 3.755 Å, 3.739 Å and 3.749 Å in plane (Table 1).

3.2. Speciation in Aqueous Solution

Before modelling the interactions of uranyl with the surface of portlandite, it is necessary to first decide which aqueous species will dominate the solute inventory. Speciation models, which include equilibrium data for $UO_2(OH)_3^-$ and $UO_2(OH)_4^{2-}$ [53], and in which CO_2/carbonate is limited, indicate that, under highly alkaline conditions (approaching the point of zero charge of portlandite at around pH 12.7 [4]), $UO_2(OH)_4^{-2}$ is likely to be the most prevalent species in solution (see the Pourbaix diagram given in Figure S2a) [54]. These predictions are in line with previous studies [55,56], although at slightly lower pH, $UO_2(OH)_3^-$ will become prevalent. EXAFS and NMR studies, as well as quantum chemical calculations, have previously studied the $[UO_2(OH)_4]^{2-}$ species and have shown it to be a stable ion [49,57–62]. Nevertheless, we shall also consider the more unusual $UO_2(OH)_5^{3-}$ ion, although this may only exist at extremely high pH [63].

In order to validate that our classical potential is able to predict the likely coordination of hydroxide ligands to uranyl, since these ligands would have the opportunity to exchange with water- or surface-bound portlandite hydroxides when forming inner-sphere adsorbed species, we have considered the following equilibria in aqueous conditions: (a) $UO_2(OH)_5^{3-}$ = $UO_2(OH)_4^{2-}$ + OH$^-$, (b) $UO_2(OH)_4^2$ = $UO_2(OH)_3^-$ + OH$^-$ and (c) $UO_2(OH)_3^-$ = $UO_2(OH)_2$ + OH$^-$. As noted in the previous section, a PMF has been computed for each of these three reactions using a coordinate corresponding to the dissociation of a hydroxyl ligand from the uranium centre. In each case, as with the sorption mechanism to portlandite, water molecules from solution are permitted to coordinate with the uranyl at every stage of the reaction but the classical potentials used do not permit protonation of any species; this is a major limitation of the model, such that the energy barriers to hydroxyl removal will likely be significantly overestimated in comparison with a real mechanism in which proton exchange would be likely. However, since the relative stability of the various hydroxyl species does not depend on the mechanistic path between them, the difference in the free energy between the bound and unbound forms in each PMF can be combined to give the relative stability of these species. The resulting PMFs for the first three equilibria are summarised in Figure 1 and clearly show that the most stable species is correctly predicted to be $UO_2(OH)_4^{2-}$, in agreement with available experimental equilibrium data.

Relative to $UO_2(OH)_4^{2-}$, species $UO_2(OH)_3^-$, $UO_2(OH)_2$ and $UO_2(OH)_5^{3-}$ are predicted to be <56 kJ·mol^{-1}, ~174 kJ·mol^{-1} and >25 kJ·mol^{-1} less stable, respectively. (More details on the aqueous complex calculations are given in the Supplementary Materials.) Taken overall, our aqueous complex calculations indicate that it is relatively easy and energetically favourable to remove the first hydroxyl group from a $UO_2(OH)_5^{3-}$ complex, but subsequent hydroxyl groups will less readily exchange for water; we therefore expect surface-adsorbed uranyl species to preferentially coordinate equatorially with four hydroxyl ligands. The high computational barriers for hydroxyl ligand exchange, either with water or surface hydroxyls, should be kept in mind in the surface-adsorption simulations since the surface species will not spontaneously or readily form inner-sphere complexes. Hence, standard molecular dynamics methods will be inappropriate to predict these species reliably, but the addition of the umbrella potential in our PMD simulations, constraining and forcibly reducing the surface to uranium distance, will encourage some ligand exchange when favourable. On the other hand, exchange of water ligands for hydroxyl is more energetically feasible and will be better described by the classical potentials, with surface hydroxyls more readily able to displace water.
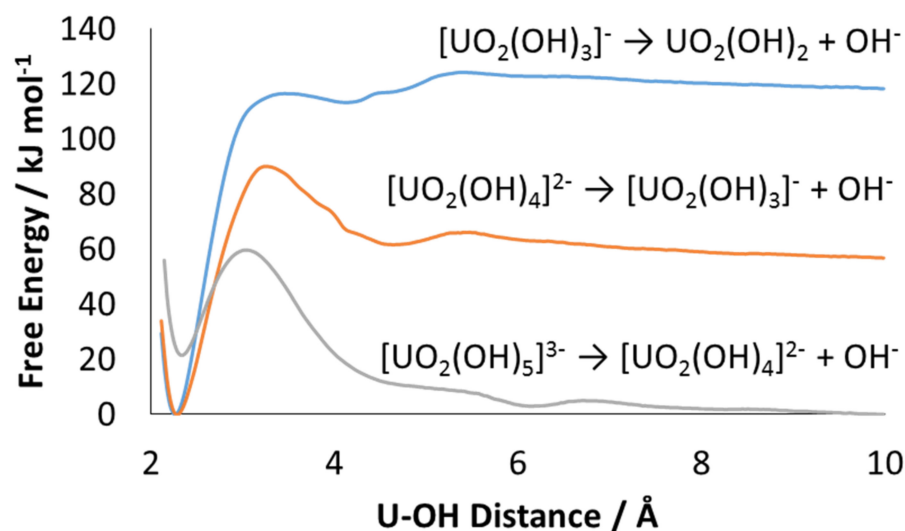
Figure 1. PMF (free energy) plots for the hydroxyl-to-water ligand exchange reaction in $[UO_2(OH)_n]^{2-n}$, (n = 3–5).

3.3. Sorption of Uranyl Hydroxides on Portlandite

In this section, PMF simulations of the free energy change of bringing six different uranyl species into close proximity to the portlandite surface will be discussed. As noted in previous sections, the barriers for hydroxyl-to-water exchanges may preclude significant exchanges in the timescales of the MD simulations and, in reality, the mechanism for sorption on portlandite and the number of OH^-/H_2O ligands involved will be highly pH-dependent. In order to capture the essence of the likely thermodynamic outcome for the uptake of uranyl, we separately considered PMF simulations involving six uranyl hydroxide species, including the thermodynamically less-favoured hydroxylated species containing water ligands. Rather than just focussing on the sorption of $UO_2(OH)_4{}^{2-}$, we have obtained surface-sorbed states for each of the species, thus accounting for species which may be produced via protonation of an OH^- group and subsequent H_2O-hydroxyl exchange near the surface. All of the bound surface species are, in principle, thermodynamically accessible, although the formation of the less-hydroxylated species would be unfavourable in a high pH environment, particularly from a kinetic perspective; therefore, those species are included simply for comparison.

To assess the importance of each surface species, the free energy of adsorption relative to the fully solvated aqueous species (for example, at a separation from the surface of >6 Å) has been obtained from the PMFs and is presented for each initial aqueous species in figure format, with the lowest energy configurations for each attached species depicted as insets on a set of free energy diagrams. In each figure, a free-energy profile is shown for adsorption to one of the three (001), (100) or (203/101) surfaces; however, the zero distance for each surface will depend on the surface topology and thus this is not directly comparable. A typical structure for each minimum energy region of the profile is shown on each figure; however, it should be noted that these are not stationary point structures and a more appropriate description in terms of the coordination numbers and positions of the peaks in the radial distribution functions are presented in Table 2 to understand the nature of the adsorbed species. In particular, the internuclear distances from the central uranium atom to three types of oxygen are shown: (a) U-OH$_{eq}$(UO$_2$), where the OH^- ligand can be attributed to the aqueous uranyl species; (b) U-OH$_{eq}$(*), where the OH^- ligand can be considered to be part of the Ca(OH)$_2$ surface; and (c) U-H$_2$O$_{eq}$, where a water molecule is coordinated to the uranyl. Figures for the first three reference species are given in the Supplementary Materials (Figures S3–S5), while those for the two species that are pertinent to an alkaline GDF-type fluid on pristine surfaces are given below in the main

text (Figures 2 and 3). Also included is a figure detailing the calculations for $UO_2(OH)_4{}^{2-}$ on defect surfaces (Figure 4).

Preliminary PMF calculations detailed the adsorption of $UO2^{2+}$ and other species with low amounts of hydroxylation, as would be expected in the near-neutral pH region, and also the $UO_2(OH)_5{}^{3-}$ hich is probably negligible under GDF conditions (see the Preliminary PMF Adsorption Calculations section of the Supplementary Materials, Figure S6). Here, we now present the calculated adsorption behaviour for the species that represent the dominant uranyl complexes to be expected in a GDF scenario.

Table 2. Analysis of the radial distribution functions from the classical simulations and PMF shown in Figures 1, 2 and S3–S6. Coordination numbers (CN) and distances (R) refer to the equatorial hydroxyl (or water) ligands of the sorbed uranyl complex and are separated into either those principally coordinated to uranyl (UO_2) or to the surface (*). The average coordination distances are shown for the principal RDF peaks obtained from windows representative of the sorbed complex. Where values are shown in parentheses, these correspond to a parallel ($\parallel$) uranyl orientation and values not in parentheses correspond to a perpendicular ($\perp$) oriented uranyl. Figures S7–S78 give details of all RDF calculations.

$Ca(OH)_2$ Surface	Aqueous Species	U-OH$_{eq}$(UO$_2$) [1]		U-OH$_{eq}$(*)		U-H$_2$O$_{eq}$		U-Ca
		CN	R (/Å)	CN	R (/Å)	CN	R (/Å)	R (/Å)
(001)	$UO_2{}^{2+}$	0 (0)	-	0 (0)	- (2.33)	5 (3)	2.53 (2.58)	6.38, 6.73 (3.68, 4.23)
	$UO_2(OH)^+$	1 (1)	2.18 (2.28)	0 (2)	- (2.28)	4 (1)	2.58 (2.58)	6.33 (4.18, 4.52)
	$UO_2(OH)_2$	2 (2)	2.23 (2.28)	0 (2)	- (2.28)	2 (0)	2.58 (-)	5.53, 5.83 (3.63, 4.28)
	$UO_2(OH)_3{}^-$	3	2.38	0	-	1	2.63	5.38, 6.13
	$UO_2(OH)_4{}^{2-}$	4	2.28	0	-	0	-	5.63, 6.03
	$UO_2(OH)_5{}^{3-}$	5	2.33	0	-	0	-	4.43, 5.82, 6.98
(100)	$UO_2{}^{2+}$	0	-	4	2.23	0	-	4.18
	$UO_2(OH)^+$	1	2.23	3	2.23	1	2.58	3.68, 4.23
	$UO_2(OH)_2$	2	2.23	1	2.23	1	2.58	3.63, 4.68
	$UO_2(OH)_3{}^-$	3	2.28	1	2.28	0	-	4.23
	$UO_2(OH)_4{}^{2-}$	3	2.28	1	-	0	-	4.13
	$UO_2(OH)_5{}^{3-}$	4	2.28	0	-	0	-	5.13
(203/101)	$UO_2{}^{2+}$	0	-	4	2.33	0	-	3.68
	$UO_2(OH)^+$	1	2.28	3	2.28	0	-	4.33
	$UO_2(OH)_2$	2	2.33	3	2.33	0	-	3.83 4.28
	$UO_2(OH)_3{}^-$	3	2.28	1	2.28	0	-	3.78, 4.33 3.73, 4.13
	$UO_2(OH)_4{}^{2-}$	4	2.28	0	-	0	-	4.13, 5.63
	$UO_2(OH)_5{}^{3-}$	5	2.33	0	-	0	-	3.83, 4.23

[1] U-OH$_{eq}$(UO$_2$) are equatorially bound OH ligands which do not form part of the surface, whereas U-OH$_{eq}$(*) corresponds to OH that is equatorially bound to U, which also remains as a part of the $Ca(OH)_2$ surface. In each case, there are also two U-O$_{ax}$ oxygens at the approximate equilibrium distance as defined by the force field for UO_2.
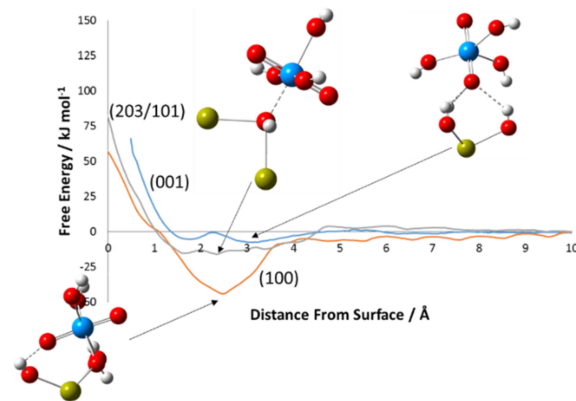
Figure 2. PMF (free energy) plots for the sorption of $[UO_2(OH)_3]^-$ to the (001), (100) and (203/101) surfaces of portlandite.

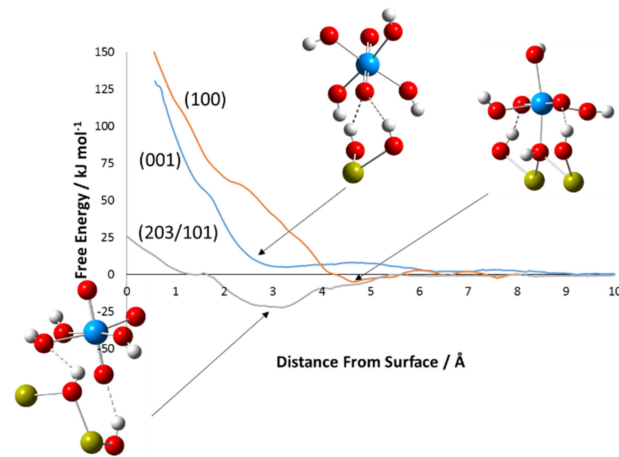**Figure 3.** PMF (free energy) plots for the sorption of $[UO_2(OH)_4]^{2-}$ to the (001), (100) and (203/101) surfaces of portlandite.

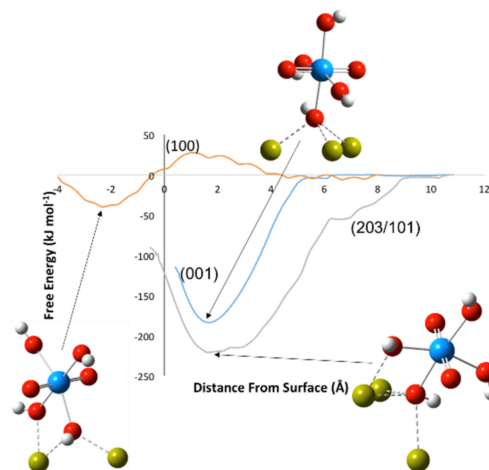**Figure 4.** PMF (free energy) plots for the sorption of $UO_2(OH)_4{}^{2-}$ to the (001), (100) and (203/101) OH-vacancy defect surfaces of portlandite.

For the case of an alkaline pH up to approximately pH 12, the species of $UO_2(OH)_3{}^-$ is expected to dominate uranyl speciation. The free energy of adsorption onto the (100) surface is most favourable for this species at -45 kJ mol^{-1} (Figure 2). $UO_2(OH)_3{}^-$ adsorbs by dissociating a water ligand from the uranium atom and coordinating to an exposed hydroxyl group in the surface, while another hydroxyl group from the complex coordinates

to two exposed calcium atoms, effectively forming a bound $UO_2(OH)_4{}^{2-}$ complex. On the (203/101) surface, a less energetically favourable (-16 kJ mol^{-1}) but similar process occurs, whereby the species dissociates a water ligand and coordinates to an exposed hydroxyl group in the surface, while one of the complex hydroxyl groups coordinates to one exposed calcium ion in the surface, thereby bridging the calcium and uranium atoms. $UO_2(OH)_3{}^{-}$ complexes show favourable adsorption to the (001) surface at approximately -7.5 kJ mol^{-1}. The most favourable configuration has uranyl binding in a perpendicular orientation with a direct interaction of the uranyl oxygen to the surface.

Above pH 12, and probably most pertinent to the hyperalkaline conditions expected in a GDF, the $UO_2(OH)_4{}^{2-}$ species needs to be considered. Figure 3 presents the PMF calculations for this critical species. Again, the (203/101) shows a distinct minimum. Here, the $[UO_2(OH)_4]^{2-}$ complex adsorbs by coordinating one of its hydroxyl groups to an exposed calcium atom in the slab, bridging it and the uranium atom, while the complex orients to form hydrogen bonds with surface hydroxyl groups. This produces the most favourable free energy change out of all three surfaces at -22 kJ mol^{-1}. Adsorption on the (100) is less favourable, with a weak minimum at ~4.7 Å distance, with adsorption proceeding by replacing a hydroxyl group from the surface (which then migrates and coordinates with two exposed calcium atoms in the surface). Adsorption onto the pristine (001) is unfavourable for this species.

Below, we summarize the general behaviour of these uranyl species on each crystallographic surface.

(001) surface: The PMFs for the sorption of $UO_2{}^{2+}$, $UO_2(OH)^{+}$, $UO_2(OH)_2$ and $UO_2(OH)_3{}^{-}$ complexes all show favourable adsorption to the surface at a PMF (collective) coordinate of ~3 Å with Ca-U distances of ~3.7 to 4.2 Å and have uranyl binding with the axial oxygens in a perpendicular orientation (with a direct interaction of a uranyl oxygen to the surface). All of the perpendicular complexes adsorb by hydrogen bonding to the surface hydroxyls and, with the exception of $UO_2(OH)_2$ (by approximately 3 kJ mol^{-1}), this is slightly more favourable than forming an inner-sphere complex. At a shorter PMF coordinate of ~1.3 Å with Ca-U distances < 5.5 Å, $UO_2{}^{2+}$, $UO_2(OH)^{+}$ and $UO_2(OH)_2$ are also able to form stable bridged inner-sphere complexes with the O=U=O parallel to the surface by exchange of equatorial water with two surface hydroxyl groups. Since the classical energies of the perpendicular and parallel sorbed complexes are very similar, they will be explored in more detail using DFT; however, the weak binding of $UO_2{}^{2+}$ and $UO_2(OH)^{+}$ suggests that they would easily desorb from the (001) surface. For $UO_2(OH)_4{}^{2-}$ and $UO_2(OH)_5{}^{3-}$, perpendicular adsorption to the (001) surface is found to be unfavourable in these calculations. $UO_2(OH)_3{}^{-}$, $UO_2(OH)_4{}^{2-}$ and $UO_2(OH)_5{}^{3-}$ are furthermore predicted to be unable to form stable parallel inner-sphere complexes.

(100) surface: The $UO_2{}^{2+}$, $UO_2(OH)^{+}$, $UO_2(OH)_2$ and $UO_2(OH)_3{}^{-}$ all show favourable adsorption to the (100) surface. The important $UO_2(OH)_4{}^{2-}$ complex and the $UO_2(OH)_5{}^{3-}$ complex both show weak sub-parallel attachment.

(203/101) surface: All considered complexes favourably absorb to the (203/101). The first three, $UO_2{}^{2+}$, $UO_2(OH)^{+}$ and $UO_2(OH)_2$, all have the ability to burrow into the surface to form a stable adsorbate. The more hydroxylated species, $UO_2(OH)_3{}^{-}$ and $UO_2(OH)_4{}^{-2}$, do not display burrowing but are still able to form stable surface species which display relatively large negative free energy changes—especially in the case of $UO_2(OH)_4{}^{-2}$, which is the most probable species to be present in a hyperalkaline fluid. Adsorption of $UO_2(OH)_5{}^{3-}$ on this surface is not favourable. Although sorption onto the fully hydroxylated (100) surface is relatively weak for $UO_2(OH)_4{}^{-2}$ and $UO_2(OH)_5{}^{3-}$, sorption of these two important species is certainly thermodynamically favourable onto the pristine (203/101) surface, where the lower density of hydroxyl ligands permits bridging and ligand exchange with the uranyl. A five-hydroxyl uranyl species is clearly less favoured, and one of its hydroxyl groups will readily dissociate if there is an available site on the surface for it to bind to. Overall, it is clear that no matter which aqueous species is considered, a four-hydroxide coordinated inner-sphere adsorbed structure would be ultimately preferred, and at high

pH, the free energy of sorption to (clean) portlandite may be in the region of approximately -20 kJ mol^{-1}, if dominated by $[UO_2(OH)_4]^{-2}$ onto (203/101) faces, as expected.

3.4. Sorption on Defect Portlandite Surfaces

Although the clean surfaces provide a useful baseline for sorption, the surface of portlandite will be quite dynamic in aqueous solutions [64]. PMF profiles for sorption of the $UO_2(OH)_4^{2-}$ complex to the (001-OH), (100-OH) and (203-OH) surfaces, where a surface OH^- has been protonated to H_2O, are shown in Figure 4. In each case, there are distinct minima corresponding to inner-sphere complexes bound by -183 kJ mol^{-1}, -40 kJ mol^{-1} and -221 kJ mol^{-1}, respectively, considerably stronger than to the clean surfaces. The radial distribution functions, summarised in Table 3, indicate that uranyl maintains a coordination number of 4 OH^- around uranium at a distance of 2.28 Å for all three surfaces and no ligand exchange. Each complex binds strongly through a direct interaction of an equatorial uranyl hydroxyl directly to one or more exposed surface calcium ions, displacing the surface water at the vacancy site. In the majority of surface complexes, the uranyl axis is oriented relatively parallel to each surface and the overall structures are similar to $UO_2(OH)_3^-$ complexes adsorbed to the clean portlandite surfaces.

Table 3. Analysis of the radial distribution functions from the classical simulations and PMF of the OH-vacancy defect surfaces shown in Figure 6. Coordination numbers (CN) and distances (R) refer to the equatorial hydroxyl (or water) ligands of the sorbed uranyl complex and are separated into either those principally coordinated to uranyl ($\approx$) or to the surface ($>$). The average coordination distances are shown for the principal RDF peaks obtained from windows representative of the sorbed complex.

Ca(OH)$_2$ Surface	Aqueous Species	U-OH$_{eq}$ ($\approx$)		U-OH$_{eq}$ ($>$)		U-Ca
		CN	R (/Å)	CN	R (/Å)	R (/Å)
(001-OH)	$UO_2(OH)_4^{2-}$	4	2.28	0	-	3.88, 4.43
(100-OH)	$UO_2(OH)_4^{2-}$	4	2.28	0	-	3.93
(203-OH)	$UO_2(OH)_4^{2-}$	4	2.28	0	-	4.13

3.5. DFT Study of the Surface Complexes

While the PMF computations provide an important quantitative assessment of the free energy change associated with bringing the various uranyl species onto the portlandite surfaces and thus give a useful overview of potential adsorbate–surface affinities, DFT computations allow us to optimize the surface geometries of possible adsorbate structures in a more robust manner. Here, we focus on the dominant aqueous species and provide details of sorbate configuration on pristine and defect (001), (100), and (203/101) surfaces. In Table 4, we present key structural details for the 12 periodic cluster models corresponding to the sorption of $UO_2(OH)_4^{2-}$ with the uranyl axis either perpendicular or parallel to the three clean (Figure 5) or three defect (Figure 6) surfaces, as observed in the classical studies. The schematic figures show the optimised complexes but omit water and the majority of the surface for clarity.

Table 4. Bond lengths and coordination numbers from the DFT-optimised structures for the (001), (100) and (203/101) surfaces and for the (001-OH), (100-OH) and (203-OH) defect surfaces.

Ca(OH)$_2$ Surface	Orientation	U-OH$_{eq}$(UO$_2$) [1]		U-OH$_{eq}$(*)		U=O	U-Ca
		CN	R (/Å)	CN	R (/Å)	R (/Å)	R (/Å)
(001)	⊥	4	2.316, 2.287, 2.244, 2.381	0	-	1.826, 1.866	5.418
	∥	4	2.228, 2.204, 2.332, 2.326	0	-	1.859, 1.879	5.060
(100)	⊥	4	2.180, 2.256, 2.307, 2.338	0	-	1.838, 1.893	5.800
	∥	3	2.221, 2.262, 2.242	1	2.238	1.867, 1.887	4.054
(203/101)	⊥	4	2.239, 2.277, 2.342, 2.306	0	-	1.836, 1.872	4.203
	∥	2	2.258, 2.281	2	2.396, 2.618	1.853, 1.868	3.977
(001-OH)	⊥	4	2.118, 2.255, 2.324, 2.368	0	-	1.866, 1.905	4.158
	∥	3	2.262, 2.254, 2.341	1	2.343	1.820, 1.858	4.082
(100-OH)	⊥	4	2.157, 2.242, 2.345, 2.348	0	-	1.869, 1.883	3.959
	∥	3	2.178, 2.251, 2.256	1	2.302	1.857, 1.900	3.508, 3.871
(203-OH)	⊥	4	2.240, 2.325, 2.341, 2.141	0	-	1.861, 1.906	3.740, 4.094
	∥	3	2.222, 2.255, 2.284	1	2.371	1.864, 1.865	3.629, 4.441

[1] U-OH$_{eq}$(UO$_2$) are equatorially bound OH ligands which do not form part of the surface, where as U-OH$_{eq}$(*) correspond to OH equatorially bound to U which also remain part of the Ca(OH)$_2$ surface. In each case the total equatorial coordination is 4 with no additional covalent H$_2$O molecules.
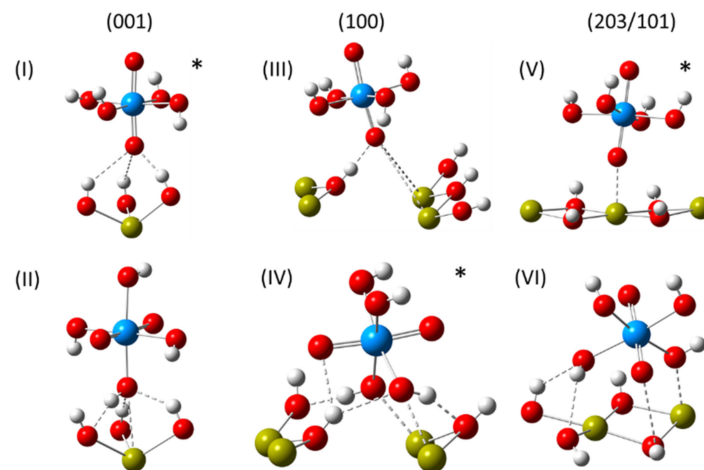

Figure 5. DFT-optimised structures of [UO$_2$(OH)$_4$]$^{2-}$ sorbed to the (001), (100) and (203/101) surfaces of portlandite. The upper structure corresponds to uranyl sorbed perpendicularly to the surface, the lower structure corresponds to uranyl sorbed parallel to the surface; the asterisk denotes the lower energy of each pair.

Figure 6. DFT-optimised structures of $[UO_2(OH)_4]^{2-}$ sorbed to the (001), (100) and (203) OH-vacancy defect surfaces of portlandite. The upper structure corresponds to uranyl sorbed perpendicularly to the surface, the lower structure corresponds to uranyl sorbed parallel to the surface; the asterisk denotes the lower energy of each pair.
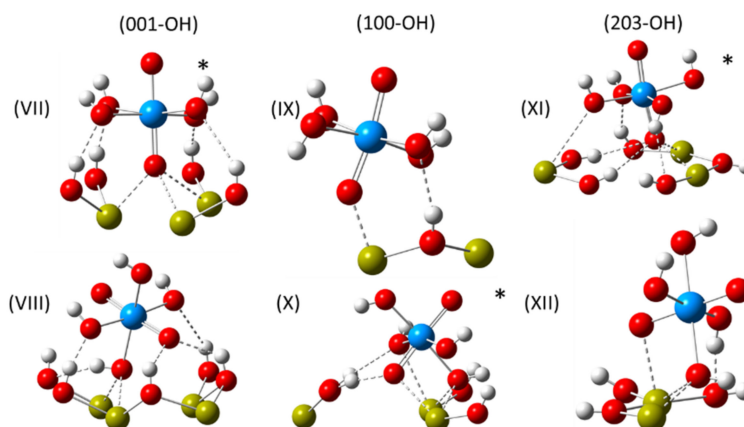
All of the optimised structures retained a uranyl equatorial coordination number of four for hydroxyl and there were no water molecules in the inner shell. For comparison with the classical PMF results, the equatorially coordinated hydroxyl groups have been partitioned into those bridging to the surface U-OH$_{eq}$(>) and those exposed to solvent, U-OH$_{eq}$($\approx$). The optimised conformations (I) to (XII) can be summarised as follows (the lower-energy configuration between each pair of possible orientations is indicated with an asterisk):

1. (001, $\perp$)*—uranyl oxygen coordinates to the hydrogen atom of a surface hydroxyl group at a distance of 1.80 Å;
2. (001, $\parallel$)—uranyl hydroxide forms two hydrogen bonds with the surface of 1.83 Å and 1.87 Å;
3. (100, $\perp$)—uranyl oxygen coordinates to the three exposed calcium ions with O-Ca distances of 2.60 Å, 2.93 Å and 3.12 Å;
4. (100, $\parallel$)*—hydroxyl from the uranyl complex substitutes for the missing surface hydroxyl group with O-Ca distances of 2.58 Å, 2.64 Å and 3.21 Å. For comparison, the hydroxyl O-Ca distance on the clean (001) surface is only 2.39 Å;
5. (203/101, $\perp$)—uranyl oxygen atom coordinates to the hydrogen atom of a surface hydroxyl group at a distance of 1.75 Å;
6. (203/101, $\parallel$)—one uranyl hydroxide group coordinates to an exposed calcium ion and is hydrogen bonded to a surface hydroxyl group with distances of 2.41 Å and 1.83 Å, respectively; a second uranyl hydroxide group also hydrogen bonds to another surface hydroxyl group at a distance of 1.78 Å;
7. (001-OH, $\perp$)*—uranyl oxygen coordinates to an exposed calcium ion at a distance of 2.40 Å;
8. (001-OH, $\parallel$)—a hydroxyl group from the uranyl complex substitutes for the missing surface hydroxyl group with O-Ca distances of 2.46 Å and 2.60 Å;
9. (100-OH, $\perp$)—uranyl oxygen coordinates to an exposed calcium atom at a distance of 2.40 Å;
10. (100-OH, $\parallel$)*—two uranyl hydroxide groups coordinate to two exposed calcium ions at distances of 2.40 Å and 2.60 Å;
11. (203-OH, $\perp$)*—uranyl oxygen atom coordinates to two exposed calcium ions at distances of 2.49 Å and 2.65 Å, replacing the missing hydroxyl group;
12. (203-OH, $\parallel$)—a hydroxyl group from the uranyl complex substitutes for the missing surface hydroxyl group with O-Ca distances of 2.56 Å and 2.66 Å, while another

hydroxyl group from the uranyl complex hydrogen bonds to a surface hydroxyl group at a distance of 1.75 Å.

The perpendicular-oriented uranyl structures to the (001) and (100) clean surfaces (>-OH) appear to be weakly interacting outer-sphere complexes with >-OH$^-$ ... O=U=O separated by 1.75–1.80 Å. For the other surfaces, including the defect surfaces, the uranyl oxygen can clearly interact more directly with surface calcium ions to form more inner-sphere-like complexes in these cases. When oriented parallel to the surface, the uranyl more clearly forms inner-sphere complexes with at least one bridging OH$^-$ at the vacancy site. The U-OH bond lengths were found to average between 2.24 Å and 2.31 Å, typical of r(U-OH) in isolated $UO_2(OH)_4^{2-}$, using the PBE functional (see Table 1). The axial U-O bond lengths were all found to average in the range of 1.84 Å to 1.89 Å. Although longer than typical U–O_{ax} lengths experimentally observed in uranyl phases (1.72–1.82 Å) and more consistent with uranate phases (1.86–1.97 Å), here, the computational value with the PBE functional is more typical of uranyl in $UO_2(OH)_4^{2-}$. Overall, it is interesting to note the long Ca-U distances in all complexes: at the lower end, in the defect (100) and (203) cases, they are shorter at 3.51 to 3.74 Å, and at the upper end, 5.06 to 5.80 Å, when perpendicular to clean (100) and (001) surfaces. The other cases fall between these extremes at 3.96 and 4.20 Å. It should be noted that the optimised structures are assumed to be local minima and it is not meaningful to consider these structures as absolute models of sorption since more extensive sampling of alternative structures was not possible at this level.

The relative potential energies of the two orientations of uranyl for each surface are compared in Table 5; however, due to the different surface compositions and the large energetic dependence on the configurations of the water molecules, it is not possible to directly compare energies between different surfaces—the values are intended to compare only the two different orientations on the same surface. In order to assess the relative interaction energy of the perpendicular ($\perp$) and parallel ($\parallel$) orientations on the same surface, we have re-computed single-point energies of the surface and uranyl complex at the DFT-optimised structure, but have omitted all of the water molecules. Thus, the energetic differences are considerably larger in magnitude than those obtained as free energies by the classical simulations since they do not include any stabilisation due to solvation. The results are quite conclusive in the prediction of favourable (gas phase) interactions of uranyl in a perpendicular relative to a parallel orientation with both the (001) and (203/101) surfaces by −33 to −39 kJ mol^{-1} and −82 to −93 kJ mol^{-1}, respectively. For the (100) surface configurations, the situation is reversed and a parallel uranyl orientation is preferred over the perpendicular by 78 to 144 kJ mol^{-1}. These findings are broadly in line with the results of the classical simulations for the full sorption of the complexes, where the (001) and (203/101) structures favour direct interaction of the surface with the uranyl oxygen. However, the DFT results predict slightly different bonding environments, with (001, $\perp$), (100, $\parallel$), and (203/101, $\perp$) whereas the PMF computations predict (001, $\parallel$), (100, $\parallel$) and (203/101, sub-parallel).

Table 5. Relative potential energies of the surface complexes excluding water molecules at the DFT(PBE)-optimised structures. The energy difference ($E(\perp)$-$E(\parallel)$) is for the perpendicular orientation relative to the parallel orientation.

Surface	Energy Difference/(kJ mol^{-1})
(001)	−38.7
(001-OH)	−33.5
(100)	78.8
(100-OH)	144.1
(203)	−82.2
(203-OH)	−93.3

3.6. Experimental EXAFS Analysis

Table 6 shows the results from fitting both the ex-situ and in-situ EXAFS data for U(VI) with hydroxylated CaO. Four sets of reaction conditions were fully analysed:

13. pH 12 in KOH, 48 h reaction time before ex situ data acquisition;
14. pH 11 with 2 mM CO_3^{2-}, pre-prepared ex situ 48 h reaction time before data acquisition;
15. pH 12 in KOH, reacted in situ, sorption for approximately 2 h before data acquisition;
16. pH 12 in LiOH, reacted in situ, sorption for approximately 2 h before data acquisition.

Table 6. Shell-by-shell fit of the experimental EXAFS of uranyl with CaO.

Experiment		U-O$_{ax}$	U-O	U-U	U-Ca(1)	U-Ca(2)
Ex situ pH 12 in KOH	CN [1]	1.7	4.5	-	1.0	1.0
	R (/Å) [2]	1.87 (0.009)	2.33 (0.01)	-	3.08 (0.011)	3.72 (0.008)
Ex situ 2 mM CO_3^{2-} pH 11	CN	2.0	5.0	-	2.0	-
	R (/Å)	1.81 (0.004)	2.29 (0.011)	-	2.91 (0.006)	-
In situ pH 12 in KOH	CN	1.6	4.1	1.0	1.0	-
	R (/Å)	1.86 (0.009)	2.35 (0.008)	3.83 (0.005)	4.08 (0.009)	-
In situ pH 12 in LiOH	CN	2.4	4.1	1.7	2.1	4.0
	R (/Å)	1.93 (0.01)	2.28 (0.007)	3.84 (0.016)	3.59 (0.002)	3.78 (0.008)

[1] Coordination number. [2] σ^2(/Å^2) is shown in parentheses.

For the in situ experiments, both XANES spectra of the U(VI)-reacted CaO (111) surfaces showed signs of broadening of the U(VI) absorption peak at the white line (Figure 7, feature A), very similar to XANES reference spectra of Ca-uranate [9] and spectra of uranates published by Bots et al. [65]. This is indicated on Figure 7 by the increase in intensity at feature 'B'. As a result, the feature in the shoulder region (feature C in Figure 7) that is typical of an undistorted U–O$_{axial}$ of the uranyl moiety disappears in both in situ experiments. This implies that the U–O$_{axial}$ bond lengths are elongated after reaction and that the U(VI) bonding environment is distorted upon reaction with the mineral surface. Undistorted uranyl has short U=O bond lengths (1.77–1.81 Å) [66], which produces the diagnostic shoulder feature clearly visible in the uranyl reference spectrum (bottom curve on Figure 7).

In both in situ experiments, the EXAFS fits (see Figure 8) confirmed a significant increase in the U–O$_{axial}$ bond lengths to between 1.86 and 1.93 Å. In addition, four to five equatorial oxygen atoms at a distance of 2.23–2.35 Å could be fitted, which supports the idea that $UO_2(OH)_4^{2-}$ is the dominant species involved in adsorption to the mineral surface. Despite the fact that all solutions were undersaturated with compreignacite ($K_2(UO_2)_6O_4(OH)_6 \cdot 7H_2O$), a further ~ four Ca atoms and 1–2 U atoms could also be fitted within the spectra. This could indicate some surface co-precipitation of U(VI). The measured CN and radial distances would be in agreement with the formation of calcium uranate phases previously published [10,65,67]. These data will be further discussed in the next section.
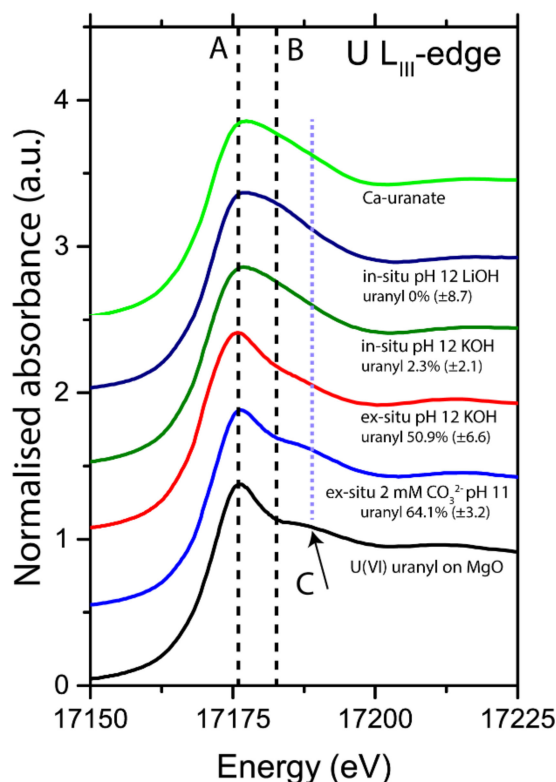
Figure 7. Experimental XANES spectra of adsorbed U(VI) on CaO (111). The reference spectrum for Ca-uranate is taken from [10]. The predicted uranyl concentrations (%) are from linear combination analyses (LCA).
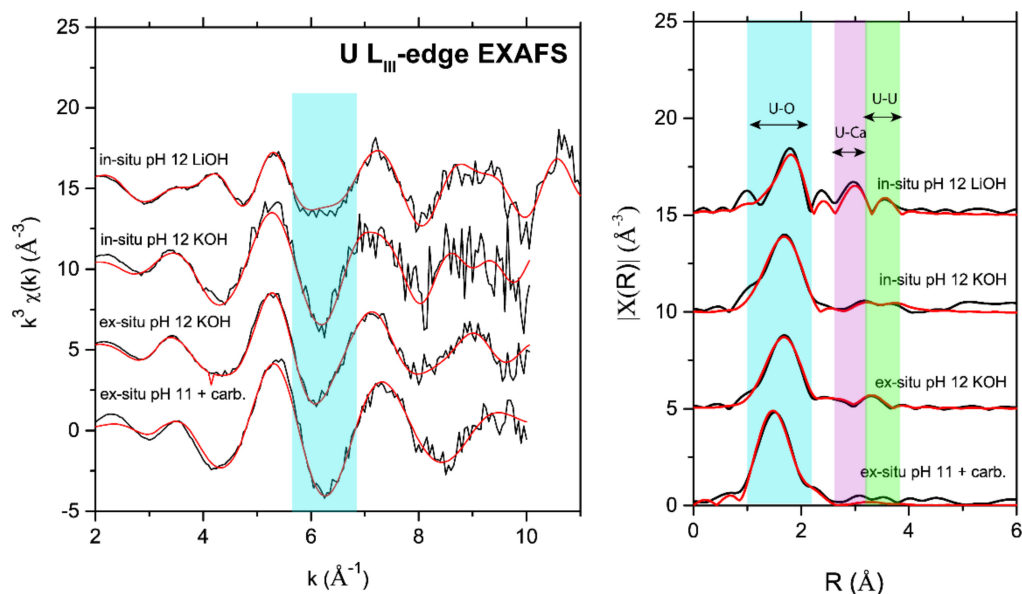

Figure 8. Analysis of the experimental EXAFS data: U LIII edge reflEXAFS (**left** panel) and the Fourier back-transformed EXAFS (**right** panel). Data are in black, modelled fit is in red.

In contrast, the ex situ spectra retain feature C (Figure 7), typical of the U=O$_{axial}$ of uranyl, especially with carbonate present. Unlike the in situ experiments, where the surface was freshly reacted and carefully rinsed, the ex situ crystal surfaces roughened significantly during reaction and were not rinsed with MilliQ water. This difference in U(VI) speciation between in situ and ex situ experiments is likely due to differences in sample preparation and surface reactivity with bulk experiments presumably retaining undistorted

bulk uranyl, whilst the in situ experiments allow for dynamic reaction of the uranate species to be identified. Linear combination fits of the XANES confirmed a mixture of uranyl and uranate with uranyl being predominantly present in the ex situ samples. This is why the XANES spectra are different; therefore, we conclude that the ex situ measurements provide less reliable configurations of adsorbed species in the presence of an aqueous fluid. We conclude that the in situ EXAFS results under equivalent conditions are more likely to give a reliable understanding of the adsorption of the uranyl–hydroxide complexes, especially with as reactive a surface as CaO(111). As shown by fitting the in situ EXAFS data (Figure 8, Table 6), adsorption of $UO_2(OH)_4^{2-}$ onto a surface equivalent to the portlandite (001) results in an adsorbate complex with elongated axial oxygen distances, discernible Ca and U backscatterers consistent with surface attachment and fourfold equatorial oxygen coordination with distances of 2.35 to 2.28 Å. All of these spectral details are consistent with the lowest energy configuration calculated by DFT on the portlandite (001) surface.

4. Discussion

The high pH experimental EXAFS data clearly fit to a coordination environment containing two shorter axial U=O bonds and four longer equatorial U-O bonds, which, as stated, is consistent with the computational predictions of both aqueous and surface complexes favouring coordination to four hydroxyl ligands. The average DFT bond lengths (1.84–1.89 Å) for the U=O bonds are close to those measured by the experimental analyses (1.86–1.93 Å), with both indicating a tendency to be longer than aqueous $[UO_2(OH)_4]^{2-}$, at 1.83 and ~1.85 Å for the experiment and the PBE functional, respectively. The calculated equatorial bonds are in very good agreement with DFT predictions in the range of 2.18–2.38 Å, again matching those from the experimental EXAFS data at 2.28–2.35 Å.

Perhaps the most important aspect of the EXAFS analyses is that the data are not consistent with the U-O environment, which would result from precipitation-deposited crystalline calcium uranate ($CaUO_4$). This is because, although calcium uranate has two distinct U-O coordination distances in its crystalline form, at 1.966 and 2.282 Å [68,69], these are distinct from the distances in uranyl. Typically, $U-O_{axial}$ bond lengths in uranate phases are within the range (1.86−1.97 Å) [10,67,70], longer than the $U-O_{axial}$ bond lengths in uranyl phases (1.70–1.82 Å) [68,69], and the $U-O_{eq}$ distances for several layered metal uranate phases have been reported within the range (2.15–2.30 Å), shorter in general than in uranyl phases (2.27–2.49 Å).

Although the in situ pH 12 (LiOH) EXAFS gives U-Ca scattering (at 3.59–3.78 Å) close to the calcium uranate system (3.653 Å), these data are also similar to the inner-sphere models predicted for uranyl sorption. U-Ca distances consistent with the experimental data are consistently predicted for a wide range of the sorption complexes observed in the classical simulations (3.68 to 4.33 Å) and in the more likely inner-sphere complexes studied by DFT (3.51 to 4.20 Å). Furthermore, the longer U-Ca value, which is observed in the other pH 12 in situ (KOH) experiment (4.08 Å), is not consistent with uranate but does match with inner-sphere DFT models. The shorter ex situ U-Ca distance (3.08 Å) is not observed in any of our sorption models but may be a result of scattering from Ca^{2+} coordinated to uranyl anionic species, such as $CaUO_2(OH)_4$. The DFT structure of $CaUO_2(OH)_4$ illustrates such a short U-Ca distance (3.14 Å).

The in situ EXAFS U-U distances at pH 12 (3.83–3.84 Å) are similar to uranate (3.850 Å) [68] and do not match uranyl minerals such as metastudtite ($UO_4.2H_2O$) [71], which has a longer U-U distance (4.21 Å). It is interesting to compare the experimental U-U data with our computational predictions where U(VI) or uranyl is incorporated within a crystalline portlandite environment. When incorporated, we predict U-Ca distances between 3.74 and 3.76 Å, at the longer end of the range seen in the in situ pH 12 (LiOH) experiment and notably longer than typical Ca-Ca distance in portlandite (3.6 Å). Although, in the incorporated models, we have not embedded two uranium species, DFT computations on the molecular uranyl dimer complex $(UO_2)_2(OH)_6^{2-}$ resulted in a U-U distance of

3.98 Å, which suggests the longer experimental values are unlikely to be due to dimeric sorption complexes.

Taking a holistic view, the U–O_{axial} experimental observations strongly suggest that U(VI) associated with the portlandite (001) surface is consistent with a mixture of uranyl and uranate-like coordination environments. The computational studies predict a range of possibly stable inner-sphere sorbed uranyl–hydroxyl complexes, particularly to (203/101) or defect surfaces, which are consistent with the experimental fit to 4 longer equatorial U-O bonds. It is also quite clear that the surface complexation at a high pH cannot be described by a single model and a range of adsorbed uranyl, incorporated uranyl and uranate precipitate are all likely to contribute to the uptake of uranium at the surface of portlandite under these experimental conditions.

5. Conclusions

Density functional theory and classical molecular dynamics calculations have been performed on various uranyl hydroxide species in the presence of water and portlandite. Uranyl has been shown to adopt a four-coordinate structure, with respect to hydroxyl groups, both in solution and when adsorbed to portlandite surfaces, consistent with experimental EXAFS data at high pH.

Although uranyl is found to only weakly adsorb to the (001) and (100) clean surfaces, significantly stronger interactions are predicted with the (203/101) surfaces prevalent under groundwater conditions, at OH-vacancy sites or on a rough surface. The uranyl ions are typically found to form sorbed species with four equatorially coordinated hydroxyl ligands with direct interaction of a uranyl oxygen with surface calcium ions in the (001) and (203/101) cases, but uranyl is likely to be sorbed more parallel to the (100) surface.

The experimental EXAFS data looking at the CaO (111) analogue of the portlandite (001) surface are largely consistent with a six-coordinate structural layer or a deposit similar to calcium uranate, although there is also strong evidence for uranyl-type coordination, as would be expected, to originate from the adsorbates predicted by the computational models. It is quite clear from the X-ray absorption experiments that the short preparation timescales of the in situ and ex situ experiments, of 2 to 48 h, respectively, indicate that the uptake of uranyl by portlandite is extremely rapid, particularly in the context of GDF timescales.

We have shown that the most strongly interacting (chemi-)sorbed/inner-sphere species will undergo some degree of ligand exchange, where the surface hydroxyls will displace the hydroxyl or water ligands of the aqueous uranyl complexes. The kinetic barriers predicted from our classical potentials of mean force utilise a U-surface distance coordinate and the potentials only allow for ligand exchange and do not allow for a mechanism involving dynamic protonation/de-protonation of the ligands. Thus, we might expect our computations to represent the upper limits of the kinetic processes.

$UO_2(OH)_4{}^{2-}$ is likely to be particularly prevalent at high pH, and our computations indicate that sorption of this species will be inversely proportional to the hydroxyl density of the surface, since the strongly sorbed surface-complexes require OH "vacancies" or exposed Ca^{2+}, which might be anticipated on the (203/101) surfaces or at lower pH; in these cases, approximate sorption free energies are predicted up to -220 kJ mol^{-1}, considerably greater than the approximately -20 kJ mol^{-1} for the clean surfaces. As other uranyl hydroxyl $\{[UO_2(OH)_n]^{2-n}$ ($n = 0$–3)$\}$ species are formed, either near the surface or at lower pH, they can more readily exchange their equatorial water ligands to form stronger bound inner-sphere complexes, even with the hydroxyl rich (001) surfaces, although, again, lower hydroxyl densities become significantly more favourable. Although we have not explicitly studied the interaction of uranyl hydroxide with the more negative (deprotonated) (001) or (100) surfaces expected at very high pH (>12.7), sorption of any of the anionic $UO_2(OH)_3{}^-$ or $UO_2(OH)_4{}^{2-}$ or even $UO_2(OH)_5{}^{3-}$ complexes would not be expected to be favourable under these conditions due to strong repulsive Coulombic forces. However, our computations would indicate that uranyl sorption would still be favourable with the lower hydroxyl density (203/101) surfaces, which are more prevalent in aqueous conditions.

Supplementary Materials: The following are available online at https://www.mdpi.com/article/10.3390/min11111241/s1: Supplementary Text on hydroxyl–water ligand exchange and Preliminary PMF Adsorption Calculations; Tables S1–S3, and Figures S1–S78. Table S1: Gas phase surface energies, Table S2: Portlandite lattice parameters, Table S3: U(VI) substituted lattice parameters, Figure S1. Comparison of the (101) [blue transparent plane] and (203) [purple transparent plane] surfaces of port-landite, showing the step difference between the two (Ca = grey, OH = red). Drawn using Vesta 3, Figure S2. (a) Uranyl speciation using MINTEQ database. Note the predominance of $UO_2(OH)_4{}^-$—above pH ~12. (b) Uranyl species predominance for a 25 ppm uranyl solution, again calculated using the MINTEQ database but showing an estimated activity for $UO_2(OH)_5$—in the pH range of interest [estimated from the ΔG values computed by Moll et al. (2014)] showing that the penta-hydroxyl species is most probably negligible in the range pH 12 to 13, Figure S3. PMF (free energy) plots for the sorption of $UO_2{}^{2+}$ to the (001), (100) and (203/101) surfaces of portland-ite, Figure S4. PMF (free energy) plots for the sorption of $[UO_2(OH)]^+$ to the (001), (100) and (203/101) surfaces of portlandite, Figure S5. PMF (free energy) plots for the sorption of $[UO_2(OH)_2]$ to the (001), (100) and (203/101) surfaces of portlandite, Figure S6. PMF (free energy) plots for the sorption of $[UO_2(OH)_5]^{3-}$ to the (001), (100) and (203/101) surfaces of portlandite, Figure S7: U-Oh RDF for the $UO_2{}^{2+}$ bridging structure on the (001) surface of portlandite, Figure S8: U-Ow RDF for the $UO_2{}^{2+}$ bridging structure on the (001) surface of portlandite, Figure S9: U-Ca RDF for the $UO_2{}^{2+}$ bridging structure on the (001) surface of portlandite, Figure S10: U-Oh RDF for $UO_2{}^{2+}$ on the (001) surface of portlandite, Figure S11: U-Ow RDF for $UO_2{}^{2+}$ on the (001) surface of portlandite, Figure S12: U-Ca RDF for $UO_2{}^{2+}$ on the (001) surface of portlandite, Figure S13: U-Oh RDF for the $UO_2(OH)^+$ bridging structure on the (001) surface of portlandite, Figure S14: U-Ow RDF for the $UO_2(OH)^+$ bridging structure on the (001) surface of portlandite, Figure S15: U-Ca RDF for the $UO_2(OH)^+$ bridging structure on the (001) surface of portlandite, Figure S16: U-Oh RDF for $UO_2(OH)^+$ on the (001) surface of portlandite, Figure S17: U-Ow RDF for $UO_2(OH)^+$ on the (001) surface of portlandite, Figure S18: U-Ca RDF for $UO_2(OH)^+$ on the (001) surface of portlandite, Figure S19: U-Oh RDF for the $UO_2(OH)_2$ bridging structure on the (001) surface of portlandite, Figure S20: U-Ow RDF for the $UO_2(OH)_2$ bridging structure on the (001) surface of portlandite, Figure S21: U-Ca RDF for the $UO_2(OH)_2$ bridging structure on the (001) surface of portlandite, Figure S22: U-Oh RDF for $UO_2(OH)_2$ on the (001) surface of portlandite, Figure S23: U-Ow RDF for $UO_2(OH)_2$ on the (001) surface of portlandite, Figure S24: U-Ca RDF for $UO_2(OH)_2$ on the (001) surface of portlandite, Figure S25: U-Oh RDF for $UO_2(OH)_3{}^-$ on the (001) surface of portlandite, Figure S26: U-Ow RDF for $UO_2(OH)_3{}^-$ on the (001) surface of portlandite, Figure S27: U-Ca RDF for $UO_2(OH)_3{}^-$ on the (001) surface of portlandite, Figure S28: U-Oh RDF for $UO_2(OH)_4{}^{2-}$ on the (001) surface of portlandite, Figure S29: U-Ow RDF for $UO_2(OH)_4{}^{2-}$ on the (001) surface of portlandite, Figure S30: U-Ca RDF for $UO_2(OH)_4{}^{2-}$ on the (001) surface of portlandite, Figure S31: U-Oh RDF for $UO_2(OH)_5{}^{3-}$ on the (001) surface of portlandite, Figure S32: U-Ow RDF for $UO_2(OH)_5{}^{3-}$ on the (001) surface of portlandite, Figure S33: U-Ca RDF for $UO_2(OH)_5{}^{3-}$ on the (001) surface of portlandite, Figure S34: U-Oh RDF for $UO_2{}^{2+}$ on the (100) surface of portlandite, Figure S35: U-Ow RDF for $UO_2{}^{2+}$ on the (100) surface of portlandite, Figure S36: U-Ca RDF for $UO_2{}^{2+}$ on the (100) surface of portlandite, Figure S37: U-Oh RDF for $UO_2(OH)^+$ on the (100) surface of portlandite, Figure S38: U-Ow RDF for $UO_2(OH)^+$ on the (100) surface of portlandite, Figure S39: U-Ca RDF for $UO_2(OH)^+$ on the (100) surface of portlandite, Figure S40: U-Oh RDF for $UO_2(OH)_2$ on the (100) surface of portlandite, Figure S41: U-Ow RDF for $UO_2(OH)_2$ on the (100) surface of portlandite, Figure S42: U-Ca RDF for $UO_2(OH)_2$ on the (100) surface of portlandite, Figure S43: U-Oh RDF for $UO_2(OH)_3{}^-$ on the (100) surface of portlandite, Figure S44: U-Ow RDF for $UO_2(OH)_3{}^-$ on the (100) surface of portlandite, Figure S45: U-Ca RDF for $UO_2(OH)_3{}^-$ on the (100) surface of portlandite, Figure S46: U-Oh RDF for $UO_2(OH)_4{}^{2-}$ on the (100) surface of portlandite, Figure S47: U-Ow RDF for $UO_2(OH)_4{}^{2-}$ on the (100) surface of portlandite, Figure S48: U-Ca RDF for $UO_2(OH)_4{}^{2-}$ on the (100) surface of portlandite, Figure S49: U-Oh RDF for $UO_2(OH)_5{}^{3-}$ on the (100) surface of portlandite, Figure S50: U-Ow RDF for $UO_2(OH)_5{}^{3-}$ on the (100) surface of portlandite, Figure S51: U-Ca RDF for $UO_2(OH)_5{}^{3-}$ on the (100) surface of portlandite, Figure S52: U-Oh RDF for $UO_2{}^{2+}$ on the (203) surface of portlandite, Figure S53: U-Ow RDF for $UO_2{}^{2+}$ on the (203) surface of portlandite, Figure S54: U-Ca RDF for $UO_2{}^{2+}$ on the (203) surface of portlandite, Figure S55: U-Oh RDF for $UO_2(OH)^+$ on the (203) surface of portlandite, Figure S56: U-Ow RDF for $UO_2(OH)^+$ on the (203) surface of portlandite, Figure S57: U-Ca RDF for $UO_2(OH)^+$ on the (203) surface of portlandite, Figure S58: U-Oh RDF for $UO_2(OH)_2$ on the (203) surface of portlandite, Figure S59: U-Ow RDF for $UO_2(OH)_2$ on the (203) surface of portlandite, Figure S60: U-Ca RDF for

$UO_2(OH)_2$ on the (203) surface of portlandite, Figure S61: U-Oh RDF for $UO_2(OH)_3{}^-$ on the (203) surface of portlandite, Figure S62: U-Ow RDF for $UO_2(OH)_3{}^-$ on the (203) surface of portlandite, Figure S63: U-Ca RDF for $UO_2(OH)_3{}^-$ on the (203) surface of portlandite, Figure S64: U-Oh RDF for $UO_2(OH)_4{}^{2-}$ on the (203) surface of portlandite, Figure S65: U-Ow RDF for $UO_2(OH)_4{}^{2-}$ on the (203) surface of portlandite, Figure S66: U-Ca RDF for $UO_2(OH)_4{}^{2-}$ on the (203) surface of portlandite, Figure S67: U-Oh RDF for $UO_2(OH)_5{}^{3-}$ on the (203) surface of portlandite, Figure S68: U-Ow RDF for $UO_2(OH)_5{}^{3-}$ on the (203) surface of portlandite, Figure S69: U-Ca RDF for $UO_2(OH)_5{}^{3-}$ on the (203) surface of portlandite, Figure S70: U-Oh RDF for $UO_2(OH)_4{}^{2-}$ on the (001-OH) surface of portlandite, Figure S71: U-Ow RDF for $UO_2(OH)_4{}^{2-}$ on the (001-OH) surface of portlandite, Figure S72: U-Ca RDF for $UO_2(OH)_4{}^{2-}$ on the (001-OH) surface of portlandite, Figure S73: U-Oh RDF for $UO_2(OH)_4{}^{2-}$ on the (100-OH) surface of portlandite, Figure S74: U-Ow RDF for $UO_2(OH)_4{}^{2-}$ on the (100-OH) surface of portlandite, Figure S75: U-Ca RDF for $UO_2(OH)_4{}^{2-}$ on the (100-OH) surface of portlandite, Figure S76: U-Oh RDF for $UO_2(OH)_4{}^{2-}$ on the (203-OH) surface of portlandite, Figure S77: U-Ow RDF for $UO_2(OH)_4{}^{2-}$ on the (203-OH) surface of portlandite, Figure S78: U-Ca RDF for $UO_2(OH)_4{}^{2-}$ on the (203-OH) surface of portlandite.

References

1. Nuclear Decommissioning Authority (NDA). *Geological Disposal: Generic Environmental Safety Case*; Main Report NDA/RWMD/021; Nuclear Decommissioning Authority (NDA): Didcot, UK, October 2010.
2. Wilson, J.; Watson, S.; Towler, G.; Limer, L. *An Assessment of Key Controls for the Disposal of Uranium Wastes*; Report QRS-1384P-R1; Nuclear Decommissioning Authority (NDA): Didcot, UK, May 2012.
3. Gaona, X.; Kulik, D.A.; Macé, N.; Wieland, E. Aqueous-solid solution thermodynamic model of U(VI) uptake in C-S-H phases. *Appl. Geochem.* **2012**, *27*, 81–95. [CrossRef]
4. El Shafei, G.M.S. The polarizing power of metal cations in (hydr) oxides. *J. Colloid Interface Sci.* **1996**, *182*, 249–253. [CrossRef]
5. Galmarini, S.; Aimable, A.; Ruffray, N.; Bowen, P. Changes in portlandite morphology with solvent composition: Atomistic simulations and experiment. *Cem. Concr. Res.* **2011**, *41*, 1330–1338. [CrossRef]
6. Galmarini, S.; Aimable, A.; Ruffray, N.; Bowen, P. Changes in portlandite morphology with solvent composition: Atomistic simulations and experiment. *Cem. Concr. Res.* **2014**, *61–62*, 71. [CrossRef]
7. Reeder, R.J.; Nugent, M.; Tait, C.D.; Morris, D.E.; Heald, S.M.; Beck, K.M.; Hess, W.P.; Lanzirotti, A. Coprecipitation of uranium(VI) with calcite: XAFS, micro-XAS, and luminescence characterization. *Geochim. Cosmochim. Acta* **2001**, *65*, 3491–3503. [CrossRef]
8. Kelly, S.D.; Rasbury, E.T.; Chattopadhyay, S.; Kropf, A.J.; Kemner, K.M. Evidence of a stable uranyl site in ancient organic-rich calcite. *Environ. Sci. Technol.* **2006**, *40*, 2262–2268. [CrossRef]
9. Tits, J.; Geipel, G.; Macé, N.; Eilzer, M.; Wieland, E. Determination of uranium(VI) sorbed species in calcium silicate hydrate phases: A laser-induced luminescence spectroscopy and batch sorption study. *J. Colloid Interface Sci.* **2011**, *359*, 248–256. [CrossRef]
10. Macé, N.; Wieland, E.; Dähn, R.; Tits, J.; Scheinost, A.C. EXAFS investigation on U(VI) immobilization in hardened cement paste: Influence of experimental conditions on speciation. *Radiochim. Acta* **2013**, *101*, 379–389. [CrossRef]

11. Chardon, E.S.; Bosbach, D.; Bryan, N.D.; Lyon, I.C.; Marquardt, C.; Römer, J.; Schild, D.; Vaughan, D.J.; Wincott, P.L.; Wogelius, R.A.; et al. Reactions of the feldspar surface with metal ions: Sorption of Pb(II), U(VI) and Np(V), and surface analytical studies of reaction with Pb(II) and U(VI). *Geochim. Cosmochim. Acta* **2008**, *72*, 288–297. [CrossRef]

12. Van Veelen, A.; Copping, R.; Law, G.T.W.; Smith, A.J.; Bargar, J.R.; Rogers, J.; Shuh, D.K.; Wogelius, R.A. Uranium uptake onto Magnox sludge minerals studied using EXAFS. *Mineral. Mag.* **2012**, *76*, 3095–3104. [CrossRef]

13. Cao, Q.; Huang, F.; Zhuang, Z.; Lin, Z. A study of the potential application of nano-Mg(OH)(2) in adsorbing low concentrations of uranyl tricarbonate from water. *Nanoscale* **2012**, *4*, 2423–2430. [CrossRef]

14. Baranek, P.; Lichanot, A.; Orlando, R.; Dovesi, R. Structural and vibrational properties of solid Mg(OH)(2) and Ca(OH)(2)— Performances of various hamiltonians. *Chem. Phys. Lett.* **2001**, *340*, 362–369. [CrossRef]

15. Kalinichev, A.G.; Kirkpatrick, R.J. Molecular dynamics modeling of chloride binding to the surfaces of calcium hydroxide, hydrated calcium aluminate, and calcium silicate phases. *Chem. Mater.* **2002**, *14*, 3539–3549.

16. Hase, Y. Computational study of the solid-state vibrations and force field of magnesium and calcium hydroxides. *J. Braz. Chem. Soc.* **2006**, *17*, 741–745. [CrossRef]

17. Laugesen, J.L. Density functional calculations of elastic properties of portlandite, Ca(OH)(2). *Cem. Concr. Res.* **2005**, *35*, 199–202. [CrossRef]

18. Busing, W.R.; Levy, H.A. Neutron Diffraction Study of Calcium Hydroxide. *J. Chem. Phys.* **1957**, *26*, 563–568. [CrossRef]

19. Petch, H.E.; Megaw, H.D. Crystal Structure of Brucite (MgOH2) and Portlandite (CaOH2) in Relation to Infrared Absorption. *J. Opt. Soc. Am.* **1954**, *44*, 744–745. [CrossRef]

20. Desgranges, L.; Grebille, D.; Calvarin, G.; Chevrier, G.; Floquet, N.; Niepce, J.-C. Hydrogen thermal motion in calcium hydroxide— Ca (OH)2. *Acta Crystallogr. Sect. B* **1993**, *49*, 812–817. [CrossRef]

21. Van Veelen, A.; Preedy, O.; Qi, J.; Law, G.T.W.; Morris, K.; Mosselmans, J.F.W.; Ryan, M.P.; Evans, N.D.M.; Wogelius, R.A. Uranium and technetium interactions with wustite [Fe1-xO] and portlandite [Ca(OH)(2)] surfaces under geological disposal facility conditions. *Mineral. Mag.* **2014**, *78*, 1097–1113. [CrossRef]

22. Pointeau, I.; Landesman, C.; Giffaut, E.; Reiller, P. Reproducibility of the uptake of U(VI) onto degraded cement pastes and calcium silicate hydrate phases. *Radiochim. Acta* **2004**, *92*, 645–650. [CrossRef]

23. Doudou, S.; Arumugam, K.; Vaughan, D.J.; Livens, F.R.; Burton, N.A. Investigation of ligand exchange reactions in aqueous uranyl carbonate complexes using computational approaches. *Phys. Chem. Chem. Phys.* **2011**, *13*, 11402–11411. [CrossRef]

24. Doudou, S.; Vaughan, D.J.; Livens, F.R.; Burton, N.A. Atomistic Simulations of Calcium Uranyl(VI) Carbonate Adsorption on Calcite and Stepped-Calcite Surfaces. *Environ. Sci. Technol.* **2012**, *46*, 7587–7594. [CrossRef]

25. Kerisit, S.; Parker, S. Free energy of adsorption of water and metal ions on the {1014} calcite surface. *J. Am. Chem. Soc.* **2004**, *126*, 10152–10161. [CrossRef]

26. Spagnoli, D.; Cooke, D.J.; Kerisit, S.; Parker, S.C. Molecular dynamics simulations of the interaction between the surfaces of polar solids and aqueous solutions. *J. Mater. Chem.* **2006**, *16*, 1997–2006. [CrossRef]

27. Greathouse, J.A.; Cygan, R.T. Molecular dynamics simulation of uranyl (VI) adsorption equilibria onto an external montmorillonite surface. *Phys. Chem. Chem. Phys.* **2005**, *7*, 3580–3586. [CrossRef]

28. Greathouse, J.A.; O'Brien, R.J.; Bemis, G.; Pabalan, R.T. Molecular dynamics study of aqueous uranyl interactions with quartz (010). *J. Phys. Chem. B* **2002**, *106*, 1646–1655. [CrossRef]

29. Kerisit, S.; Liu, C. Diffusion and Adsorption of Uranyl Carbonate Species in Nanosized Mineral Fractures. *Environ. Sci. Technol.* **2012**, *46*, 1632–1640. [CrossRef]

30. Kerisit, S.; Liu, C. Molecular Dynamics Simulations of Uranyl and Uranyl Carbonate Adsorption at Aluminosilicate Surfaces. *Environ. Sci. Technol.* **2014**, *48*, 3899–3907. [CrossRef]

31. Freeman, C.L.; Harding, J.H.; Cooke, D.J.; Elliott, J.A.; Lardge, J.S.; Duffy, D.M. New forcefields for modeling biomineralization processes. *J. Phys. Chem. C* **2007**, *111*, 11943–11951. [CrossRef]

32. Abascal, J.L.F.; Vega, C. A general purpose model for the condensed phases of water: TIP4P/2005. *J. Chem. Phys.* **2005**, *123*, 234505. [CrossRef]

33. *Materials Studio v6.1.200*; Accelrys Software Inc.: San Diego, CA, USA, 2012.

34. Smith, W.; Forester, T.R. DL_POLY_2.0: A general-purpose parallel molecular dynamics simulation package. *J. Mol. Graph.* **1996**, *14*, 136–141. [CrossRef]

35. Bonomi, M.; Branduardi, D.; Bussi, G.; Camilloni, C.; Provasi, D.; Raiteri, P.; Donadio, D.; Marinelli, F.; Pietrucci, F.; Broglia, R.A.; et al. PLUMED: A portable plugin for free-energy calculations with molecular dynamics. *Comput. Phys. Commun.* **2009**, *180*, 1961–1972. [CrossRef]

36. Hoover, W.G. Canonical dynamics: Equilibrium phase-space distributions. *Phys. Rev. A* **1985**, *31*, 1695–1697. [CrossRef] [PubMed]

37. Williams, C.D.; Burton, N.A.; Travis, K.P.; Harding, J.H. The Development of a Classical Force Field to Determine the Selectivity of an Aqueous Fe3+-EDA Complex for TcO4- and SO42-. *J. Chem. Theory Comput.* **2014**, *10*, 3345–3353. [CrossRef]

38. Kumar, S.; Rosenberg, J.M.; Bouzida, D.; Swendsen, R.H.; Kollman, P.A. Multidimensional free-energy calculations using the weighted histogram analysis method. *J. Comput. Chem.* **1995**, *16*, 1339–1350. [CrossRef]

39. Dimelow, R.J.; Bryce, R.A.; Masters, A.J.; Hillier, I.H.; Burton, N.A. Exploring reaction pathways with transition path and umbrella sampling: Application to methyl maltoside. *J. Chem. Phys.* **2006**, *124*, 114113. [CrossRef]

40. CP2K Developer Group 2000–2015. Available online: https://www.cp2k.org/ (accessed on 5 November 2021).

41. Perdew, J.P.; Burke, K.; Ernzerhof, M. Generalized gradient approximation made simple. *Phys. Rev. Lett.* **1996**, *77*, 3865–3868. [CrossRef]

42. Goedecker, S.; Teter, M.; Hutter, J. Separable dual-space Gaussian pseudopotentials. *Phys. Rev. B* **1996**, *54*, 1703–1710. [CrossRef]

43. Hartwigsen, C.; Goedecker, S.; Hutter, J. Relativistic separable dual-space Gaussian pseudopotentials from H to Rn. *Phys. Rev. B* **1998**, *58*, 3641–3662. [CrossRef]

44. Krack, M. Pseudopotentials for H to Kr optimized for gradient-corrected exchange-correlation functionals. *Theor. Chem. Acc.* **2005**, *114*, 145–152. [CrossRef]

45. Lippert, G.; Hutter, J.; Parrinello, M. A hybrid Gaussian and plane wave density functional scheme. *Mol. Phys.* **1997**, *92*, 477–487. [CrossRef]

46. Frisch, M.J.; Trucks, G.W.; Schlegel, H.B.; Scuseria, G.E.; Robb, M.A.; Cheeseman, J.R.; Scalmani, G.; Barone, V.; Petersson, G.A.; Nakatsuji, H.; et al. *Gaussian 09*; Gaussian, Inc.: Wallingford, CT, USA, 2016.

47. Zhao, Y.; Truhlar, D. The M06 suite of density functionals for main group thermochemistry, thermochemical kinetics, noncovalent interactions, excited states, and transition elements: Two new functionals and systematic testing of four M06-class functionals and 12 other functionals. *Theor. Chem. Acc.* **2008**, *120*, 215–241.

48. Küchle, W.; Dolg, M.; Stoll, H.; Preuss, H. Ab initio pseudopotentials for Hg through Rn: I. Parameter sets and atomic calculations. *Mol. Phys.* **1991**, *74*, 1245–1263. [CrossRef]

49. Shamov, G.A.; Schreckenbach, G. Theoretical study of the oxygen exchange in uranyl hydroxide. An old riddle solved? *J. Am. Chem. Soc.* **2008**, *130*, 13735–13744. [CrossRef]

50. Moll, H.; Reich, T.; Szabó, Z. The hydrolysis of dioxouranium(VI) investigated using EXAFS and O-17-NMR. *Radiochim. Acta* **2000**, *88*, 411. [CrossRef]

51. Parkhurst, D.L.; Appelo, C.A.J. User's guide to PHREEQC (Version 2): A computer program for speciation, batch-reaction, one-dimensional transport, and inverse geochemical calculations. *Water-Resour. Investig. Rep.* **1999**, *99*, 312.

52. Newville, M.; Ravel, B.; Haskel, D.; Rehr, J.J.; Stern, E.A.; Yacoby, Y. Analysis of multiple-scattering XAFS data using theoretical standards. *Phys. B Condens. Matter* **1995**, *208–209*, 154–156. [CrossRef]

53. Guillaumont, R.; Fanghänel, T.; Fuger, J.; Grenthe, I.; Neck, V.; Palmer, D.A.; Rand, M.H. *Update on the Chemical Thermodynamics of Uranium, Neptunium, Plutonium, Americium and Technetium*; Elsevier: Amsterdam, The Netherlands, 2003.

54. *The Geochemist's Workbench 2021*; Rockware: Golden, CO, USA; Available online: https://www.gwb.com/ (accessed on 5 November 2021).

55. Kienzler, B.; Luckscheiter, B.; Wilhelm, S. Waste form corrosion modeling: Comparison with experimental results. *Waste Manag.* **2001**, *21*, 741–752. [CrossRef]

56. Langmuir, D. *Aqueous Enviromental Geochemistry*; Prentice-Hall Inc.: Upper Saddle River, NJ, USA, 1997.

57. Vallet, V.; Wahlgren, U.; Schimmelpfennig, B.; Moll, H.; Szabó, Z.; Grenthe, I. Solvent effects on uranium(VI) fluoride and hydroxide complexes studied by EXAFS and quantum chemistry. *Inorg. Chem.* **2001**, *40*, 3516–3525. [CrossRef]

58. Szabó, Z.; Grenthe, I. On the Mechanism of Oxygen Exchange Between Uranyl(VI) Oxygen and Water in Strongly Alkaline Solution as Studied by O-17 NMR Magnetization Transfer. *Inorg. Chem.* **2010**, *49*, 4928–4933. [CrossRef]

59. Farkas, I.; Bányai, I.; Szabó, Z.; Wahlgren, U.; Grenthe, I. Rates and mechanisms of water exchange of UO_2^{2+}(aq) and UO2(oxalate)F(H2O)(2)(-): A variable-temperature O-17 and F-19 NMR study. *Inorg. Chem.* **2000**, *39*, 799–805. [CrossRef]

60. Wahlgren, U.; Moll, H.; Grenthe, I.; Schimmelpfennig, B.; Maron, L.; Vallet, V.; Gropen, O. Structure of uranium(VI) in strong alkaline solutions. A combined theoretical and experimental investigation. *J. Phys. Chem. A* **1999**, *103*, 8257–8264. [CrossRef]

61. Schreckenbach, G.; Hay, P.J.; Martin, R.L. Theoretical study of stable trans and cis isomers in [UO2(OH)(4)](2-) using relativistic density functional theory. *Inorg. Chem.* **1998**, *37*, 4442–4451. [CrossRef]

62. Sonnenberg, J.L.; Hay, P.J.; Martin, R.L.; Bursten, B.E. Theoretical investigations of uranyl-ligand bonding: Four- and five-coordinate uranyl cyanide, isocyanide, carbonyl, and hydroxide complexes. *Inorg. Chem.* **2005**, *44*, 2255–2262. [CrossRef]

63. Clark, D.L.; Conradson, S.D.; Donohoe, R.J.; Keogh, D.W.; Morris, D.E.; Palmer, P.D.; Rogers, R.D.; Tait, C.D. Chemical speciation of the uranyl ion under highly alkaline conditions. Synthesis, structures, and oxo ligand exchange dynamics. *Inorg. Chem.* **1999**, *38*, 1456–1466. [CrossRef]

64. Nordstrom, D.K.; Plummer, L.N.; Langmuir, D.; Busenberg, E.; May, H.M.; Jones, B.F.; Parkhurst, D.L. Revised Chemical Equilibrium Data for Major Water—Mineral Reactions and Their Limitations. In *Chemical Modeling of Aqueous Systems II*; American Chemical Society: Washington, DC, USA, 1990; Chapter 31; Volume 416, pp. 398–413.

65. Bots, P.; Morris, K.; Hibberd, R.; Law, G.T.W.; Mosselmans, J.F.W.; Brown, A.P.; Doutch, J.; Smith, A.J.; Shaw, S. Uranium(VI) Colloidal Nanoparticles in Conditions Relevant to Radioactive Waste Disposal. *Langmuir* **2014**, *30*, 14396–14405. [CrossRef]

66. Thompson, H.A.; Brown, G.E., Jr.; Parks, G.A. XAFS spectroscopic study of uranyl coordination in solids and aqueous solution. *Am. Mineral.* **1997**, *82*, 483–496. [CrossRef]

67. Catalano, J.G.; Brown, G.E., Jr. Analysis of uranyl-bearing phases by EXAFS spectroscopy: Interferences, multiple scattering, accuracy of structural parameters, and spectral differences. *Am. Mineral.* **2004**, *89*, 1004–1021. [CrossRef]

68. Matar, S.F.; Demazeau, G. Electronic band structure of CaUO4 from first principles. *J. Solid State Chem.* **2009**, *182*, 2678–2684. [CrossRef]

69. Loopstra, B.O.; Rietveld, H.M. Structure of Some Alkaline-Earth Metal Uranates. *Acta Crystallogr. Sect. B* **1969**, *25*, 787–791. [CrossRef]

70. King, R.B. Some aspects of structure and bonding in binary and ternary uranium(VI) oxides. *Chem. Mater.* **2002**, *14*, 3628–3635. [CrossRef]
71. Deliens, M.; Piret, P. Metastudtite, UO4. 2H2O, a new mineral from Shinkolobwe, Shaba, Zaire. *Am. Mineral.* **1983**, *68*, 456–458.